

OPEN ACCESS

Potential Dependent Mn Oxidation and Its Role in Passivation of $\text{Ni}_{38}\text{Fe}_{20}\text{Cr}_{22}\text{Mn}_{10}\text{Co}_{10}$ Multi-Principal Element Alloy Using Multi-Element Resolved Atomic Emission Spectroelectrochemistry

To cite this article: Junsoo Han *et al* 2021 *J. Electrochem. Soc.* **168** 051508

Manuscript version: Accepted Manuscript

Accepted Manuscript is “the version of the article accepted for publication including all changes made as a result of the peer review process, and which may also include the addition to the article by IOP Publishing of a header, an article ID, a cover sheet and/or an ‘Accepted Manuscript’ watermark, but excluding any other editing, typesetting or other changes made by IOP Publishing and/or its licensors”

This Accepted Manuscript is© .



This is an open access article distributed under the terms of the Creative Commons Attribution 4.0 License (CC BY, <http://creativecommons.org/licenses/by/4.0/>), which permits unrestricted reuse of the work in any medium, provided the original work is properly cited.

View the [article online](#) for updates and enhancements.

**Potential Dependent Mn Oxidation and Its Role in
Passivation of Ni₃₈Fe₂₀Cr₂₂Mn₁₀Co₁₀ Multi-Principal
Element Alloy Using Multi-Element Resolved Atomic
Emission Spectroelectrochemistry**

Journal:	<i>Journal of The Electrochemical Society</i>
Manuscript ID	JES-103658.R1
Manuscript Type:	Research Paper
Date Submitted by the Author:	21-Apr-2021
Complete List of Authors:	HAN, Junsoo; University of Virginia, Center for Electrochemical Science and Engineering Li, Xuejie; Chimie-ParisTech, PSL University, IRCP-CNRS Gerard, Angela; University of Virginia, Materials Science and Engineering Lu, Pin; QuesTek Innovations LLC Saal, James; QuesTek Innovations LLC Frankel, Gerald; The Ohio State University, Fontana Corrosion Center; Ogle, Kevin; Chimie-Paristech, PSL, IRCP-CNRS Scully, John; University of Virginia, Materials Science and Engineering
Keywords:	Multi-principal element alloy, Passivation, AESEC, XPS, EIS

SCHOLARONE™
Manuscripts

1
2
3 1 **Potential Dependent Mn Oxidation and Its Role in Passivation of Ni₃₈Fe₂₀Cr₂₂Mn₁₀Co₁₀**
4
5 2 **Multi-Principal Element Alloy Using Multi-Element Resolved Atomic Emission**
6
7 3 **Spectroelectrochemistry**
8
9
10 4

11
12 5 Junsoo Han,^{1,z} Xuejie Li,² Angela Y. Gerard,¹ Pin Lu,³ James E. Saal,⁴ Gerald S. Frankel,^{5,*}
13

14
15 6 Kevin Ogle,² and John R. Scully^{1,*}
16

17 7 ¹Department of Materials Science and Engineering, University of Virginia, Charlottesville,
18
19 8 Virginia 22904, USA

20
21 9 ²Chimie ParisTech, PSL Research University, CNRS, Institut de Recherche Chimie Paris (IRCP),
22
23 10 F-75005 Paris, France

24
25
26 11 ²QuesTek Innovations LLC, Evanston, Illinois 60201, USA

27
28 12 ⁴Citrine Informatics, Redwood City, California 94063, USA

29
30
31 13 ⁵Fontana Corrosion Center, The Ohio State University, Columbus, Ohio 43210, USA

32
33 14 *Electrochemical Society Fellow.

34 15 ^zE-mail: junsoo.han@chimieparistech.psl.eu
35
36 16

37
38 17 **Abstract**

39
40 18 The identity of passivating oxides on multi-principal element alloys is of great interest as their
41
42 19 optimization offers the potential for exceptional corrosion resistance in aqueous solutions over a
43
44 20 broad range of potential and pH. This study focuses on a non-equiatomic Ni₃₈Fe₂₀Cr₂₂Mn₁₀Co₁₀
45
46 21 solid solution alloy and tracks the fate of each alloying element during linear sweep voltammetry,
47
48 22 low and intermediate potential holds in the passive potential domain as well as during open circuit
49
50 23 relaxation after anodic polarization in slightly acidified Cl⁻ solution. Ni dissolves at all potentials,
51
52 24 Fe and Co are incorporated into oxides or hydroxides in low concentrations whilst Cr and Mn are
53
54
55
56
57
58
59
60

1
2
3 25 enriched at passive potentials. At low passivating potentials, Mn(II) dissolves and is incorporated
4
5 26 in minor amounts in oxides containing large concentrations of Cr(III). Considerable enrichment in
6
7 27 Mn(II)-species occurs relative to Cr(III) in the oxide at 0.1 V vs. SCE. Electrochemical impedance
8
9 28 spectroscopy suggests the presence of layered oxides with marginal passivation at high Mn(II)
10
11 29 levels. The formation of these oxides depends on a combination of thermodynamic and kinetic
12
13 30 factors as well as the sequence of passivation.
14
15

16
17 31 *This paper is part of the JES Focus Issue on Characterization of Corrosion Processes in Honor of*
18 32 *Philippe Marcus.*
19 33

21 34 **Introduction**

22
23
24 35 Multi-principal element alloys (MPEAs) have exhibited a range of outstanding mechanical
25
26 36 properties as well as promising catalytic attributes [1, 2]. In some cases, emerging information on
27
28 37 high corrosion resistance of the MPEAs [3, 4] suggests the possibility of utilization in harsh
29
30 38 environments. For instance, these materials may be considered for nuclear waste container
31
32 39 applications [5] due to potentially high corrosion resistance, high strength, and thermal/radiation-
33
34 40 damage resistance [6, 7]. In contrast to conventional corrosion resistant alloys [8, 9], MPEAs enjoy
35
36 41 a large compositional design space because of the possible formation of a single solid solution or
37
38 42 two-phase structure over a range of alloying element compositions [10]. Single phase MPEAs are
39
40 43 attributed to the high mixing entropy, which can enhance solid solution phase stability and
41
42 44 chemical homogeneity [4, 11]. Other factors such as grain orientation, short range order vs.
43
44 45 random solid solution, interfacial properties, and interphase heterogeneity undoubtedly affect
45
46 46 corrosion but have yet to be explored extensively.
47
48
49
50

51 47 Given the large concentrations of all principal elements in equiatomic alloys (possibly
52
53 48 greater than 20 at.% for 5 elements or less), there is high potential for passive film formation due
54
55
56
57

1
2
3 49 to either dominant single element containing near-stoichiometric or complex oxides at a variety of
4
5 50 potentials, pH levels and in various electrolytes as suggested by potential-pH (E-pH) diagrams [8].
6
7
8 51 However, material design for corrosion resistance remains unclear as both scientific details and
9
10 52 figures of merit and are uncertain [10]. Identifying the contribution of the individual alloying
11
12 53 elements to the passivation and dissolution resistance of the MPEAs is critical to understanding
13
14 54 the corrosion behavior of the MPEAs. In this study, we explore one specific alloy within the Fe-
15
16 55 Ni-Co-Cr-Mn MPEA system which is a well reported system with significant metallurgy, high
17
18 56 temperature oxidation and aqueous corrosion data existing in the literature [12, 13, 14, 15, 16, 17].
19
20

21 For Cr containing MPEAs, Cr(III) enrichment in the oxide film has been observed [18, 19].
22
23 58 Cr is often considered to be the main element contributing to the stable passive film formation in
24
25 59 numerous transition metal alloys, as in the case of conventional Ni-Cr alloys and stainless steel
26
27 60 [20, 21, 22]. Cr_2O_3 has one of the lowest free energies of formation of the single element oxides
28
29 61 in binary as well as Cr-Mn-Ni-Co-Fe MPEAs [23]. Moreover, thermodynamic calculations suggest
30
31 62 Cr-based corundum and spinel oxides hosting multi-element solid solutions are the most stable
32
33 63 oxide phases over broad E-pH regions [8, 24]. Corundum $(\text{Fe, Cr})_2\text{O}_3$, spinel $(\text{Fe, Ni, Cr, Mn,}$
34
35 64 $\text{Co})_3\text{O}_4$, cubic $(\text{Co, Fe})_2\text{O}_3$, and $(\text{Ni, Mn})_2(\text{Ni, Mn, O})_3$ oxide solid solutions with space group Ia3
36
37 65 (prototype cubic Mn_2O_3), are stable over large portions of the E-pH diagram for a particular
38
39 66 $\text{Ni}_{38}\text{Fe}_{20}\text{Cr}_{22}\text{Mn}_{10}\text{Co}_{10}$ MPEA [24]. However, Cr containing MPEAs have sometimes been found
40
41 67 to possess inferior corrosion resistance compared to stainless steels [25]. Reports of both high and
42
43 68 low corrosion resistance and high or low Cr-based oxide concentrations in oxides in similar Ni-
44
45 69 Fe-Cr-Mn-Co MPEAs render any blanket generalizations regarding corrosion protection afforded
46
47 70 by Cr alloying as untenable [25, 26, 27, 28, 29].
48
49
50
51
52
53
54
55
56
57

1
2
3 71 The role of Mn in the alloys is relatively less well understood. Mn has been added to the
4
5 72 stainless steel as it is a well-known austenite stabilizing element [30], and also attractive for
6
7 73 designing face-centered cubic (FCC) MPEAs. However, formation of MnS inclusions causes
8
9 74 significant degradation in corrosion resistance of the stainless steel [31, 32, 33]. The effect of Mn
10
11 75 on high temperature oxidation of both Fe-Mn-Cr and MPEAs is relatively well established [27,
12
13 76 34, 35]. It is noteworthy that multi-phase oxides of Cr and Mn in Fe alloys are relatively less
14
15 77 protective than Cr oxides without Mn during high temperature oxidation, attributed to fast Mn
16
17 78 cation transport across Mn oxides and surface enrichment with attendant Mn depletion in the
18
19 79 underlying alloy [27, 30, 31]. Voids, spalling, and destabilization of the FCC alloy are also
20
21 80 observed during high temperature ($T > 600^{\circ}\text{C}$) oxidation of Ni-Fe-Cr-Mn-Co MPEAs [14, 36, 37,
22
23 81 38].

24
25
26
27
28 82 Adding Mn to Fe-Ni-Co-Cr single phase alloys is uniformly detrimental across a variety
29
30 83 of alloys, electrolytes and passivating procedures aside from the benefit of stabilizing the FCC
31
32 84 solid solution. For instance, adding Mn to an equimolar Cr-Fe-Co-Ni MPEA resulted in more
33
34 85 severe pitting corrosion than without Mn in 0.1 M NaCl [26] and poor passivation in 0.1 M H_2SO_4
35
36 86 solution [25, 27]. Yang *et al.* compared Fe-Ni-Co-Cr alloys with and without Mn and observed
37
38 87 that the presence of Mn resulted in degraded film stability and decreased electrochemical
39
40 88 impedance at low frequency in a 0.1 M H_2SO_4 solution. Rodriguez *et al.* investigated a series of
41
42 89 $(\text{FeNiCo})_{1-x-y}(\text{Cr})_x(\text{Mn})_y$ alloys ranging from $x + y = 0.23$ to 0.40 (in molar fraction), in a pH = 4,
43
44 90 3.5 wt.% NaCl solution at $T = 40^{\circ}\text{C}$ [29].¹ They found that alloying with a Mn content greater

53
54
55
56
57
58
59
60
¹ In these alloys the Fe, Co, and Ni contents change with modifications in Cr + Mn, but the combination of FeCoNi was always maintained at or above 60 at.% although the individual concentrations of Fe, Co, and Ni could vary and were not necessarily 1:1:1. Moreover, while the exact at.% varies in all cases, the other consideration is that very little Fe, Co and Ni were found in the passive film.

1
2
3 91 than 13–15 at.% resulted in decreased corrosion performance with higher corrosion current
4
5 92 density, and lower pitting potential. The least corrosion resistant alloy contained no Cr while
6
7
8 93 incorporating 25 at.% Mn. In spite of all the composition variations a critical threshold Cr at.%
9
10 94 could not be estimated, however, it was found that high Mn was detrimental to the passivity. That
11
12 95 said, a $\text{Ni}_{38}\text{Fe}_{20}\text{Cr}_{22}\text{Mn}_{10}\text{Co}_{10}$ MPEA exhibited similar passivation behavior to Ni-20 at.% Cr [28]
13
14
15 96 in 0.1 M NaCl at pH = 4. It is noteworthy that Mn content was, in this case, only 10 at.%.

16
17 97 Mn undergoes anodic oxidation readily as Mn^{2+} in an acidic solution at potentials below
18
19 98 the reversible potentials for both water and oxygen reduction, according to thermodynamic
20
21
22 99 predictions [24, 39]. This prediction has been experimentally demonstrated: Mn was depleted in
23
24 100 the passive film of the 304 austenitic stainless steel in 2.0 M H_2SO_4 monitored by atomic emission
25
26 101 spectroelectrochemistry (AESEC) [40]. Mn-based oxides were characterized in the passive film
27
28
29 102 by X-ray photoelectron spectroscopy (XPS) after 6 h immersion in 10 wt.% H_2SO_4 in the case of
30
31 103 Fe-xMn (x = 0.7, 2.0, and 5.0 wt.%) alloys [30]. It was concluded that the addition of 5.0 wt.%
32
33
34 104 Mn to the steel resulted in the formation of a protective oxide, which increased the corrosion
35
36 105 resistance characterized by electrochemical measurements [30]. For Fe-18Cr-xMn alloys (x = 0,
37
38 106 6, and 12 wt.%) in a 0.1 M NaCl solution at pH = 2, the passive film formed for the higher Mn
39
40
41 107 content alloy resulted in a lower E_{pit} [31], indicative of the less protective oxide. It was concluded
42
43 108 that Mn additions may suppress the passivation process by reducing the activity of adsorbed Cr
44
45 109 species. The correlation between high or low Mn content in oxides on corrosion behavior may
46
47
48 110 depend on alloy, environment, passivation steps, and most importantly, low vs. high potentials. At
49
50 111 low passivating potentials, Cr-rich oxides were observed with some Mn incorporation [31].
51
52 112 However, at higher potentials, more Mn oxides were seen coincident with the thermodynamic
53
54
55 113 stability of Mn_3O_4 , Mn_2O_3 , or Mn-containing spinels over a broader pH range [24, 28]. Concerning

1
2
3 114 Cr, one study found Cr oxide contents lower than the alloy composition, and in another study much
4
5 115 higher Cr oxide content even at high anodic potentials [25, 41].
6

7
8 116 A more comprehensive understanding of the role of Mn and Cr is required to understand
9
10 117 its role in the corrosion resistance of FCC MPEAs that often incorporate these elements. The first
11
12 118 step in this process is to track the fate of alloyed Mn in the altered layer as well as the inner and
13
14 119 outer layers of the passive films along with Cr.
15

16
17 120 We began our studies with a limited investigation into a single-phase
18
19 121 $\text{Ni}_{38}\text{Fe}_{20}\text{Cr}_{22}\text{Mn}_{10}\text{Co}_{10}$ MPEA alloy for simplicity in the Ni-Fe-Cr-Mn-Co family as previously
20
21 122 reported [28]. Tracking methods in both oxide and solution are required with elemental specificity.
22
23 123 XPS considering core level analysis and outer shell studies has been shown to be necessary [41].
24
25 124 AESEC is used for mechanistic investigation of MPEAs as it directly measures the elemental
26
27 125 dissolution rate of each alloying elements coupled with all AC and DC electrochemical
28
29 126 measurements. This technique is useful, in particular, for the selective dissolution in multi-phase
30
31 127 alloys [42] and passivation of Ni-based alloys [22, 43, 44, 45, 46]. It was recently deployed to
32
33 128 examine a nearly equiatomic Al-Ti-V-Cr MPEA in Cl⁻-containing media [47, 48], equiatomic Co-
34
35 129 Cr-Fe-Mn-Ni in 0.1 M H_2SO_4 [25], and non-equiatomic Ni-Cr-Fe-Ru-Mo-W in 2.0 M H_2SO_4 [49].
36
37 130 In combination with *ex-situ* XPS surface characterization of the outer layers of oxidized surfaces,
38
39 131 AESEC provides a powerful approach to understand the fate of each alloying element.
40
41
42
43
44

45 132 In this work, the fate of the alloying elements, whether dissolved in the solution, or
46
47 133 remaining at the surface (in the oxide or metal), was investigated for a $\text{Ni}_{38}\text{Fe}_{20}\text{Cr}_{22}\text{Mn}_{10}\text{Co}_{10}$
48
49 134 MPEA in 0.1 M NaCl, at pH = 4.0. It is generally observed that Cr is enriched in the passive film
50
51 135 in the case of Ni-Cr alloys as well as stainless steels [20, 21, 22]. Cr enrichment during the early
52
53 136 stages of passivation was previously monitored by mass-balance calculation *via* AESEC,
54
55
56
57
58
59
60

1
2
3 137 confirmed by *ex-situ* XPS and 3D-atom probe tomography (3D-APT) for a $\text{Ni}_{38}\text{Fe}_{20}\text{Cr}_{22}\text{Mn}_{10}\text{Co}_{10}$
4
5 138 MPEA in 0.1 M NaCl at pH = 4.0 [28]. However, for the Fe-Ni-Co-Cr-Mn MPEAs, either Cr
6
7
8 139 depletion or enrichment has been reported in the passive films under different conditions [19, 29].
9
10 140 In this work, we demonstrate that Mn in a $\text{Ni}_{38}\text{Fe}_{20}\text{Cr}_{22}\text{Mn}_{10}\text{Co}_{10}$ MPEA showed potential
11
12 141 dependent oxide enrichment in 0.1 M NaCl at pH = 4.0. Elements dissolved or accumulated in an
13
14 142 oxidized state at the surface for a given potential were observed by *in-situ* AESEC and *ex-situ* XPS
15
16 143 experiments. These were correlated with AC and DC electrochemistry and discussed in the context
17
18 144 of thermodynamic and kinetic oxide factors controlling oxide composition. Potential dependent
19
20 145 Mn enrichment in oxides was found to reduce the electrochemical impedance of the oxides formed
21
22
23 146 and lower corrosion resistance.
24
25
26 147

28 148 **Experimental**

30 149 *Materials*

32
33 150 The $\text{Ni}_{38}\text{Fe}_{20}\text{Cr}_{22}\text{Mn}_{10}\text{Co}_{10}$ MPEA was produced using a computational design approach
34
35 151 and characterized in our previous work [9]. A $\text{Ni}_{78}\text{Cr}_{22}$ binary alloy was also investigated for
36
37 152 comparison. All alloys were arc-melted, then solution heat treated at $T = 1100^\circ\text{C}$ for 96 h followed
38
39 153 by water quenching. The alloy exhibited a compositionally homogeneous single-phase FCC
40
41 154 characterized by energy dispersive spectroscopy (EDS) mapping and X-ray diffractometry (XRD).
42
43 155 The sample surface was initially degreased with isopropanol in an ultrasonic bath for 15 min,
44
45 156 rinsed with deionized (DI) water (MilliporeTM, 18.2 M Ω cm), and then dried with flowing N_2 . The
46
47 157 sample surface was ground with SiC paper up to P4000 under DI water then dried by flowing N_2
48
49 158 again. The 0.1 M NaCl electrolyte was prepared from analytical grade materials in DI water. The
50
51 159 final electrolyte pH was adjusted to 4.0 by adding small amounts of 1.0 M HCl solution. The
52
53
54
55
56
57
58
59
60

1
2
3 160 electrolyte pH was chosen to represent a slightly acidic corrosive environment based on the
4
5 161 thermodynamic simulation [24]. At this pH, thermodynamically stable soluble species of the
6
7 162 alloying elements as well as non-soluble species will be present in a wide potential range. This pH
8
9 163 is aggressive to challenge and interrogate passivity under conditions that were not benign, for
10
11 164 comparison for stainless steel. The electrolyte was deaerated by bubbling Ar gas for 30 min prior
12
13 165 to and during the experiments. All the experiments presented in this work showed reproducible
14
15 166 results from at least three repeated experiments.
16
17
18

19 167

20 21 168 *AESEC technique*

22
23
24 169 The elemental dissolution rate of each alloy component of the MPEA during the
25
26 170 electrochemical test was monitored *in-situ*, by the AESEC technique. The principles and detailed
27
28 171 calculations used in this technique are available elsewhere [45, 50]. The sample was placed
29
30 172 vertically in a specially designed electrochemical flow cell [51] where the released cations were
31
32 173 transferred within the electrolyte to an Ultima 2C Horiba Jobin-Yvon inductively coupled plasma
33
34 174 atomic emission spectrometer (ICP-AES). A reference electrode (saturated calomel electrode,
35
36 175 SCE) and a counter electrode (Pt foil) were positioned in a reservoir separated from the working
37
38 176 electrode by a porous membrane enabling ionic current to pass between the two compartments but
39
40 177 which prevented bulk mixing [45, 50].
41
42
43

44 178 A Gamry Reference 600TM was used for the electrochemical tests. The ICP-AES data
45
46 179 acquisition system was specially adapted to measure the analog current and potential signals from
47
48 180 the potentiostat in the same data file as the dissolved elemental emission intensities to facilitate
49
50 181 the direct comparison between spectroscopic and electrochemical data [45].
51
52
53

54 182

183 *Data analysis*

184 The detailed data analysis of the AESEC technique is presented elsewhere [45]. The
 185 elemental concentration, C_M , was calculated from the atomic emission intensity, $I_{M, \lambda}$, at a
 186 characteristic wavelength of the element, λ , measured by the ICP spectrometer as:

$$187 \quad C_M = (I_{M, \lambda} - I_{M, \lambda}^{\circ}) / \kappa_{\lambda} \quad [1]$$

188 where $I_{M, \lambda}^{\circ}$ is the background signal and κ_{λ} is the sensitivity factor for a given element, obtained
 189 from a standard ICP calibration method. The elemental dissolution rate per unit area, v_M , can be
 190 calculated from C_M with the flow rate (f) of the electrolyte controlled by a peristaltic pump and the
 191 exposed surface area A as:

$$192 \quad v_M = f C_M / A \quad [2]$$

193 It is often convenient to present the elemental dissolution rate as an equivalent elemental current
 194 density (j_M) using Faraday's law:

$$195 \quad j_M = z_M F v_M / M_M \quad [3]$$

196 where M_M is the atomic weight of M , F is the Faraday constant, and z_M is the valence of the
 197 dissolving ions for oxidation such as $M \rightarrow M^{z^+} + z_M e^-$. The oxidation states of the dissolved M in
 198 0.1 M NaCl, pH = 4 environment are assumed from thermodynamic prediction as Ni(II), Fe(II),
 199 Cr(III), Mn(II), and Co(II) [24]. It is often convenient to present the normalized elemental current
 200 densities (j_M') based on the bulk composition relative to j_{Ni} as:

$$201 \quad j_M' = j_M (z_{Ni} X_{Ni} / z_M X_M) \quad [4]$$

202 where X_M is the mass fraction of the element in the bulk alloy. Congruent dissolution is indicated
 203 when $j_M' = j_{Ni}$; otherwise non-congruent dissolution is suggested. When $j_M' < j_{Ni}$, M is being

204 retained as a corrosion product or does not completely oxidize while when $j_M' > j_{Ni}$ preferential
205 dissolution of M is indicated.

206 The total quantity of dissolved element M, $Q_M(t)$, may be calculated as:

$$207 \quad Q_M(t) = \int_0^t v_M(t) dt \quad [5]$$

208 The quantity of the excess element M remained at the surface (Θ_M) relative to Ni was calculated
209 by a mass-balance as:

$$210 \quad \Theta_M(t) = [(X_M / X_{Ni}) Q_{Ni}(t)] - Q_M(t) \quad [6]$$

211 It is worth mentioning that the interference between AESEC intensity signals of Fe (259.94
212 nm) and Mn (257.61 nm) were assessed by an individual experiment using the ICP-AES method
213 in the case of a standard solutions of known concentration. The interference of Fe signal to Mn
214 was found to be negligible (< 0.6 %), therefore, Fe and Mn signals were not corrected in this work.

216 *X-ray photoelectron spectroscopy (XPS)*

217 The samples were characterized *ex-situ* by XPS using PHI-VersaProbe IIITM X-ray
218 photoelectron spectrometer using an Al K α X-rays (1468.7 eV) under analysis pressure less than
219 10^{-8} bar. A survey of XPS was conducted with a pass energy of 224 eV to obtain the maximum
220 number of counts. A pass energy of 26 eV was used for the high-resolution spectra. XPS spectra
221 was analyzed with KOLXPDTM software. Both XPS 2p and 3p core level spectra were obtained to
222 characterize the sample surface after the electrochemical tests. The 3p core level peak analysis has
223 an advantage in this work because the 2p peaks for Ni-Fe-Cr-Mn-Co MPEA have interference
224 with the Auger transitions from some of the other alloying elements [41].

226 *Electrochemical analysis*

227 The electrochemical impedance spectroscopy (EIS) was conducted after potentiostatic
228 experiments at a given potential for 4000 s (not coupling with AESEC) in the frequency range
229 from 10^5 to 10^{-2} Hz. Potentiostatic EIS was carried out at a given potential after a potentiostatic
230 hold for 4000 s at that potential, following to a cathodic reduction step at -1.3 V vs. SCE for 600
231 s. The data were recorded with 8 points per decade using a $10 \text{ mV}_{\text{rms}}$ sine wave perturbation. The
232 electrolyte resistance (R_e) was corrected from the real part of impedance (R_p) before the Bode plot
233 construction for graphical analysis of constant-phase element (CPE) parameters [52] as well as
234 circuit model fitting.

235 The linear sweep voltammetry (LSV) was performed with following procedure; 1) a
236 constant potential at $E_{\text{ap}} = -1.3 \text{ V}$ vs. SCE was applied for 600 s to minimize the effect of air-
237 formed oxide; 2) the potential was swept from -1.3 V to 0.8 V vs. SCE with 0.5 mV s^{-1} scan rate;
238 and 3) spontaneous dissolution rate during open circuit exposure as well as open circuit potential
239 were recorded.

241 Results

242 *Elemental dissolution rates during upward potential sweep*

243 Fig. 1 reports the elementally resolved polarization data enabled by coupling AESEC with
244 conventional DC linear sweep voltammetry (LSV), denoted as AESEC-LSV. The results are
245 presented for the $\text{Ni}_{38}\text{Fe}_{20}\text{Cr}_{22}\text{Mn}_{10}\text{Co}_{10}$ MPEA in deaerated 0.1 M NaCl at $\text{pH} = 4.0$. The
246 normalized elemental dissolution rates (j_M') are presented as equivalent dissolution current
247 densities to facilitate comparison (Eqs. 3 and 4) with the net anodic or cathodic electrical current
248 density, j_e , from the potentiostat. Fig. 2 shows a close-up in the vicinity of the zero-current potential
249 ($E_{j=0}$) in the LSV.

1
2
3 250 Prior to the AESEC-LSV, a constant potential of $E_{ap} = -1.3$ V vs. SCE was applied for 600
4
5
6 251 s to minimize the pre-existing air-formed oxide. All five elemental dissolution rates showed two
7
8 252 distinctive elemental dissolution rate peaks in the cathodic reduction step, indicating that the
9
10 253 dissolution was associated with the electrochemical process. This was distinct from the
11
12 254 perturbations of the j_e signal which may be related to the hydrogen evolution reaction as shown
13
14
15 255 for other Ni-based alloys and an MPEA in a similar potential range [22, 44].
16

17 256 The AESEC-LSV results in the potential range from -0.7 V to 0.3 V vs. SCE are magnified
18
19 257 in Fig. 2 including active and passive potential domains. The Ni dissolution equivalent current
20
21 258 density, j_{Ni} , is shown as a dashed curve to indicate what the congruent dissolution rate of each
22
23 259 element would be assuming complete Ni dissolution as described in the experimental section. The
24
25 260 onset of anodically polarized elemental dissolution occurred slightly below $E_{j=0}$, near -0.46 V vs.
26
27 261 SCE. The sum of j_M ($j_{\Sigma} = j_{Ni} + j_{Fe} + j_{Cr} + j_{Mn} + j_{Co}$) is also presented in the top panel of Fig. 2. j_e is
28
29 262 the equivalent faradaic electrical current density obtained by potentiostat, simultaneously with the
30
31 263 AESEC elemental dissolution rates (j_M). The formation of oxides is suggested by $j_{\Sigma} < j_e$ while $j_{\Sigma} >$
32
33 264 j_e may be due to either a significant cathodic current or a non-electrochemical dissolution
34
35 265 mechanism. For $E > E_{j=0}$, two anodic peaks were observed near $E = -0.25$ V (a_1) and $E = -0.15$ V
36
37 266 vs. SCE (a_2). The total elemental dissolution was nearly faradaic indicated by $j_{\Sigma} \approx j_e$ at higher
38
39 267 potentials near a_2 . At potentials above a_2 , the formation of a passive film was indicated by $j_{\Sigma} < j_e$
40
41 268 in the passive potential domain. Selective Ni, Fe and Co dissolution is suggested in the passive
42
43 269 potential domain where $j_M' = j_{Ni}$ ($M = Ni, Fe, \text{ and } Co$), while non-congruent Mn and Cr dissolution
44
45 270 is indicated by $j_M' < j_{Ni}$ ($M = Mn \text{ and } Cr$). The latter may be due to the accumulation of oxidized
46
47 271 Mn, and Cr species on the surface, probably in a form of oxide or hydroxide. In the potential
48
49
50
51
52
53
54
55
56
57
58
59
60

272 domain above the passive range (Figs. 1 and 2), Mn and Cr continued to exhibit non-congruent
273 dissolution as shown in the passive domain.

274 After AESEC-LSV, the spontaneous elemental dissolution rates and the corresponding
275 open circuit potential were recorded (Fig. 1). Monitoring elemental dissolution rate in this period
276 can give insight into the elements joining the passive film formed during the polarization
277 experiment and subsequent relaxation [22, 44, 53]. Only Mn showed less than congruent
278 dissolution ($j_{\text{Mn}}' < j_{\text{Ni}}$) in this period suggesting a continual build-up of Mn on the surface during
279 the E_{oc} relaxation.

280

281 *Elemental dissolution and passivation at a constant potential*

282 Two potentials in the passive potential domain were chosen from Fig. 2 (*i.e.*, 0.0 V and 0.1
283 V vs. SCE). AESEC chronoamperometry (AESEC-CA, Fig. 3) was conducted while the net anodic
284 current was monitored from the potentiostat. Previously, a significant Cr enrichment in the early
285 stage of passivation was observed at a more negative potential ($E_{\text{ap}} = -0.25$ V vs. SCE) in the same
286 electrolyte for the $\text{Ni}_{38}\text{Fe}_{20}\text{Cr}_{22}\text{Mn}_{10}\text{Co}_{10}$ MPEA [28].

287 Fig. 3(a) gives the AESEC-CA at $E_{\text{ap}} = 0.0$ V vs. SCE with j_{M}' , j_{e} and j_{Σ} measured after a
288 cathodic potential hold for 600 s. The complete elemental oxidation was not accounted for by
289 dissolution shown as $j_{\text{e}} > j_{\Sigma}$, which may indicate passive film formation. j_{e} as well as j_{M} approach
290 stable values, indicative of a steady state between passive film formation and dissolution. Mn and
291 Cr showed non-congruent dissolution with $j_{\text{M}}' < j_{\text{Ni}}$ (dashed line) for the initial 100 s indicating
292 their retention on the surface. Non-congruent Cr dissolution was also observed ($j_{\text{Cr}}' < j_{\text{Ni}}$)
293 throughout the AESEC-CA experiment indicating a continuous Cr-species surface accumulation.

1
2
3 294 For $E_{ap} = 0.1$ V vs. SCE (Fig. 3(b)), passive film formation is again suggested by $j_{\Sigma} < j_e$. In
4
5
6 295 this case, however, passive film dissolution or local breakdown and pitting may be faster than
7
8 296 oxide formation as both j_e and j_M' increased with time. Cr and Mn again showed non-congruent
9
10 297 dissolution as both j_{Cr}' and j_{Mn}' were lower than j_{Ni} throughout the measurement. This is in
11
12 298 agreement with the previous AESEC-LSV curve (Figs. 1 and 2) where non-congruent Cr and Mn
13
14 299 dissolution were observed at 0.1 V vs. SCE, indicating Cr- and Mn-based passive film formation.
15
16

17
18 300 Further insight into the surface enrichment (Θ_M) may be obtained by the mass-balance of
19
20 301 AESEC results calculated from Eq. 6, shown in Fig. 4. At $E_{ap} = 0.0$ V vs. SCE, the excess amount
21
22 302 of oxidized Cr (Θ_{Cr}) increased with time to approximately 150 ng cm^{-2} after 4000 s. At $E_{ap} = 0.1$
23
24 303 V vs. SCE (Fig. 4(b)) the Θ_{Cr} was approximately 500 ng cm^{-2} , and $\Theta_{Mn} \approx 290 \text{ ng cm}^{-2}$ at the end
25
26 304 of the experiment. The fraction of the excess alloying element at the surface during the AESEC-
27
28 305 CA experiment is estimated from Fig. 4, and shown in Fig. 5. In both cases, Cr enrichment occurred
29
30 306 in early stage of passivation (after several hundred seconds) in accordance with previous
31
32 307 observation [28]. Mn accumulation was much greater at $E_{ap} = 0.1$ V vs. SCE where the excess Mn
33
34 308 at the surface increased as a function of time (Fig. 5(b)).
35
36
37
38
39
40
41

310 *Dissolution and passivation kinetics at each potential compared to the Ni-Cr binary alloy*

42
43
44 311 The electrochemical response of the $\text{Ni}_{38}\text{Fe}_{20}\text{Cr}_{22}\text{Mn}_{10}\text{Co}_{10}$ MPEA was compared with that
45
46 312 of a Ni-Cr binary alloy with the same at.% of Cr to investigate the effect of minor alloying elements
47
48 313 such as Mn or Co. The electrical current density as a function of potential (LSV) is shown in Fig.
49
50 314 6(a), and the current density decay during a constant potential hold in the passive domain is given
51
52 315 in Fig. 6(b). The dissolution and passivation kinetics during the potential hold experiments were
53
54 316 investigated by potentiostatic EIS as shown in Fig. 7. The j_e in the cathodic potential domain in
55
56
57
58
59
60

1
2
3 317 the LSV curve (Fig. 6(a)) for the $\text{Ni}_{38}\text{Fe}_{20}\text{Cr}_{22}\text{Mn}_{10}\text{Co}_{10}$ MPEA was lower than that of $\text{Ni}_{78}\text{Cr}_{22}$
4
5 318 binary alloy. The $\text{Ni}_{78}\text{Cr}_{22}$ binary alloy showed an anodic peak at a slightly more positive potential
6
7 319 than that of the $\text{Ni}_{38}\text{Fe}_{20}\text{Cr}_{22}\text{Mn}_{10}\text{Co}_{10}$ MPEA.
8
9

10 320 Fig. 6(b) gives the j_e decay (in log-scale both j_e and time) as a function of time when a
11
12 321 constant potential of either 0.0 V or 0.1 V vs. SCE was applied to the two alloys after 600 s of
13
14 322 cathodic potential hold at $E_{\text{ap}} = -1.3$ V vs. SCE. The j_e decay for the $\text{Ni}_{38}\text{Fe}_{20}\text{Cr}_{22}\text{Mn}_{10}\text{Co}_{10}$ MPEA
15
16 323 showed multiple metastable oxide breakdown events indicated by anodic perturbations in j_e for t
17
18 324 > 80 s at both applied potentials, whereas the $\text{Ni}_{78}\text{Cr}_{22}$ binary alloy showed much fewer and lower
19
20 325 perturbations in j_e .
21
22
23
24

25 326 EIS was conducted after a potentiostatic hold for 4000 s at $E_{\text{ap}} = 0.0$ V and 0.1 V vs. SCE,
26
27 327 after a cathodic potential hold for 600 s at -1.3 V vs. SCE. These experiments provide insights into
28
29 328 the dissolution kinetics as well as a possible oxide layer formation verified or corroborated
30
31 329 independently by a simplified equivalent electrical circuit model, as shown in Figs. 7 and 8. The
32
33 330 Bode plots and fitting results are presented in Fig. 7(a). Layered oxide circuit models were used to
34
35 331 simulate the effect of a duplex oxide, as reported for a near equiatomic Ni-Fe-Cr-Mn-Co MPEA
36
37 332 following high temperature oxidation [36, 54, 55] and aqueous passivation at room temperature
38
39 333 [26, 27, 41]. For a $\text{Ni}_{38}\text{Fe}_{20}\text{Cr}_{22}\text{Mn}_{10}\text{Co}_{10}$ MPEA at $E_{\text{ap}} = 0.0$ V vs. SCE [27, 41] and $\text{Ni}_{78}\text{Cr}_{22}$
40
41 334 binary alloy [43, 56, 57], a two time-constant circuit model with constant-phase elements (CPE)
42
43 335 was used; CPE_1/R_1 represents the inner oxide and CPE_2/R_2 represents the outer oxide, shown in
44
45 336 Fig. 8(a). For the $\text{Ni}_{38}\text{Fe}_{20}\text{Cr}_{22}\text{Mn}_{10}\text{Co}_{10}$ MPEA at $E_{\text{ap}} = 0.1$ V vs. SCE, a circuit model with a
46
47 337 relatively compact porous inner covered by an outer layer [58, 59] was utilized (Fig. 8(b)). The
48
49 338 $\text{CPE}_{1,1}$ represents the CPE contribution of the inner oxide, $R_{1,1}$ is the inner oxide resistance within
50
51
52
53
54
55
56
57
58
59
60

1
2
3 339 the pore length, CPE_{dl} is the double layer component at the interface in parallel with a faradaic
4
5
6 340 impedance (Z_F), and $CPE_{1,2}/R_{1,2}$ represents a thin outer oxide layer. Both circuits could be
7
8
9 341 reasonably well fitted to the experimental data shown in Fig. 7. For the $Ni_{38}Fe_{20}Cr_{22}Mn_{10}Co_{10}$
10
11 342 MPEA at $E_{ap} = 0.1$ V vs. SCE, the modulus impedance (Z_{mod}) in the low-frequency domain ($f <$
12
13 343 10^{-1} Hz, Fig. 7(b)) was three orders of magnitude lower than that observed for $E_{ap} = 0.0$ V vs. SCE.
14
15
16 344 This was likely due to the formation of less protective Mn oxide as previously indicated by a non-
17
18 345 congruent Mn dissolution, Figs. 3(b) and 4(b), at this potential. Lower Z_{mod} in the low-frequency
19
20 346 domain at $E_{ap} = 0.1$ V vs. SCE was also monitored for the $Ni_{78}Cr_{22}$ binary alloy (Fig. 7(b)) as
21
22 347 compared to that at $E_{ap} = 0.0$ V vs. SCE. For the $Ni_{78}Cr_{22}$, the difference in Z_{mod} between two
23
24 348 applied potentials was only one order of magnitude. The inner oxide resistance ($R_{i,1}$) of the
25
26 349 $Ni_{38}Fe_{20}Cr_{22}Mn_{10}Co_{10}$ MPEA at $E_{ap} = 0.1$ V vs. SCE obtained from the circuit model fitting using
27
28 350 Fig. 8(b) was $160 \Omega \text{ cm}^2$ whereas that the inner oxide resistance ($R_{i,1}$) at $E_{ap} = 0.0$ V vs. SCE was
29
30 351 $1.2 \times 10^5 \Omega \text{ cm}^2$ using Fig. 8(a). This may indicate a less protective oxide at $E_{ap} = 0.1$ V vs. SCE
31
32 352 compared to that at $E_{ap} = 0.0$ V vs. SCE for the $Ni_{38}Fe_{20}Cr_{22}Mn_{10}Co_{10}$ MPEA.
33
34
35
36
37
38
39
40

353

354 *Passive film characterization by XPS*

41
42
43 355 The surface of the $Ni_{38}Fe_{20}Cr_{22}Mn_{10}Co_{10}$ MPEA after each potentiostatic hold experiment
44
45 356 was characterized by *ex-situ* XPS, shown in Figs. 9 and 10. Analyzing the 2p XPS data for a Ni-
46
47 357 Fe-Cr-Mn-Co based MPEA is difficult due to the overlap of 2p and Auger transitions [41]. To this
48
49 358 end, the high-resolution XPS 3p core level spectra were obtained from 35 to 80 eV, shown in Fig.
50
51 359 10.
52
53
54
55
56
57
58
59
60

1
2
3 360 The Cr 2p_{3/2} spectra were analyzed because there is no interference between 2p Auger
4
5 361 transitions from the other elements and 2p photoelectron signal of Cr. At both applied potentials,
6
7
8 362 the Cr 2p_{3/2} spectra could be fitted by Cr(0) metallic (574.2 eV), Cr(III) hydroxide (577.3 eV), and
9
10 363 Cr(III) oxide (576.2 eV) peaks [60]. For Mn, the XPS 2p core level spectrum near 640 eV binding
11
12 364 energy is sometimes explored to examine Mn(II) or Mn(III), and Mn-oxide species [61, 62].
13
14 365 However, this binding energy largely overlaps with the Ni Auger signal [41], which makes both
15
16 366 quantitative and qualitative analysis of Mn 2p difficult. A shoulder in the peak of the Mn 2p
17
18 367 photoelectron spectrum near 655 eV for the Ni₃₈Fe₂₀Cr₂₂Mn₁₀Co₁₀ MPEA polarized to 0.1 V vs.
19
20 368 SCE was observed, which does not have any interference with Ni Auger transitions. This may
21
22 369 indicate the presence of Mn(II) species, possibly a Mn-oxide [63]. This peak was not observed for
23
24 370 the Ni₃₈Fe₂₀Cr₂₂Mn₁₀Co₁₀ MPEA at E_{ap} = 0.0 V vs. SCE. The suggestion of minimal Mn-based
25
26 371 oxide formation at this potential is consistent with the AESEC results shown in Figs. 3 and 4.
27
28
29
30

31 372 The XPS 3p core level spectrum of the Ni₃₈Fe₂₀Cr₂₂Mn₁₀Co₁₀ MPEA shows distinct peaks
32
33 373 indicative of the presence of Mn-oxide species at E_{ap} = 0.1 V vs. SCE (Fig. 10(b)). A Mn metallic
34
35 374 peak at 47.0 eV and a Mn oxide peak at 48.6 eV, possibly attributed to Mn(II) [64], were similarly
36
37 375 characterized by the XPS 3p analysis of a near equiatomic Ni-Fe-Cr-Mn-Co MPEA [41]. At E_{ap} =
38
39 376 0.0 V vs. SCE (Fig. 10(a)), only a Mn metallic peak was detected.
40
41
42
43
44

45 378 **Discussion**

46 379 *The role of Mn and Cr*

47
48
49 380 In this work, it is posited that Mn has a detrimental effect on the passivity of the
50
51 381 Ni₃₈Fe₂₀Cr₂₂Mn₁₀Co₁₀ MPEA in a 0.1 M NaCl, at pH = 4 solution. The effect is potential-
52
53 382 dependent and degrades the corrosion resistance of Ni₃₈Fe₂₀Cr₂₂Mn₁₀Co₁₀ MPEA compared to a
54
55
56
57
58
59
60

1
2
3 383 Ni₇₈Cr₂₂ binary alloy under the same conditions. EIS and DC electrochemistry of
4
5 384 Ni₃₈Fe₂₀Cr₂₂Mn₁₀Co₁₀ MPEA indicated that a change in potential from 0.0 V to 0.1 V vs. SCE was
6
7 385 more detrimental to the passive film than the same potential applied to a Ni₇₈Cr₂₂ binary alloy. As
8
9
10 386 a consequence, increased instability of the passive film (j_e decay as a function of time punctuated
11
12 387 with breakdown events, Fig. 6(b)) and lowered Z_{mod} (and the inner oxide resistance, Fig. 7) are
13
14
15 388 consistent with XPS 3p characterization (Fig. 10), which corroborates with the AESEC mass-
16
17 389 balance to indicate excess Mn at the surface (Figs. 4 and 5).

18
19 390 The results herein demonstrate that Mn can congruently dissolve or remain on the surface
20
21 391 depending on the applied potential in the passive potential domain of the Ni₃₈Fe₂₀Cr₂₂Mn₁₀Co₁₀
22
23 392 MPEA in a 0.1 M NaCl at pH = 4 solution. A layered oxide is indicated by EIS analysis using a
24
25
26 393 circuit model fit, similar to previous observation in the case of an equiatomic Ni-Fe-Cr-Mn-Co
27
28 394 MPEA in 0.05 M H₂SO₄ [41]. The cation release detected at $E_{ap} = 0.0$ V vs. SCE suggested nearly
29
30
31 395 congruent elemental dissolution rates for Ni, Fe, Co, and Mn but not for Cr, accounting for Cr
32
33 396 enrichment in the oxide (Fig. 3(a)). The surface did not reach a stable state at $E_{ap} = 0.1$ V vs. SCE
34
35
36 397 as indicated by both j_e and j_M increasing as a function of time (Fig. 3(b)). At $E_{ap} = 0.1$ V vs. SCE,
37
38 398 nearly congruent dissolution of Ni, Fe and Co was observed. In contrast, Cr and Mn dissolution
39
40
41 399 was found to be non-congruent. For an equiatomic Ni-Fe-Cr-Mn-Co MPEA, both the natively
42
43 400 formed oxide and electrochemically formed passive film were characterized to have an outer Cr,
44
45 401 Fe and Co-based oxide, and an inner Cr- and Mn-based oxide as analyzed by the XPS 3p core level
46
47 402 spectra and time of flight-secondary ion mass spectroscopy (ToF-SIMS) [41]. A strong segregation
48
49
50 403 of Cr and Mn in the presence of O on the surface and in oxide phases is predicted for the Cr-Mn-
51
52 404 Fe-Co-Ni MPEA by an *ab initio* thermodynamic simulation [23]. The result at $E_{ap} = 0.1$ V vs. SCE
53
54
55 405 may be explained by this thermodynamic prediction assuming the outer Cr-, Fe-, and Co-based
56
57
58
59
60

oxide layer dissolved at least partially at this potential whereas the inner Cr- and Mn-based oxides remained (Fig. 3(b)) due to the strong low segregation free energy of Cr and Mn [23].

It should be noted that the Cr oxide formation and congruent Mn dissolution at $E_{ap} = 0.0$ V vs. SCE observed in Fig. 3 is in accordance with the thermodynamic predictions for the same MPEA composition and electrolyte used in this work [24]. However, the apparent build-up of Mn at $E_{ap} = 0.1$ V vs. SCE contradicts the thermodynamic calculations which predicted that Mn would be completely oxidized to soluble Mn^{2+} over a broad potential range at $pH = 4$ [24]. The thermodynamically stable formation of $(Fe,Cr)_2O_3$ was predicted due to the low mixing Gibbs energy of Cr_2O_3 and Fe_2O_3 . In contrast, Mn_2O_3 mixing on the corundum lattice was not favored [24]. Limited Fe_2O_3 formation, if any, and non-congruent Mn dissolution was observed by AESEC at $E_{ap} = 0.1$ V vs. SCE (Fig. 3(b)). Therefore, it can be speculated that Mn-based oxides such as MnO, Mn_2O_3 , Mn_3O_4 , or a $MnCr_2O_4$ spinel are more likely possibilities in this system at this potential. Except for the spinel, these oxides are not likely mixed with Cr_2O_3 . These Mn oxides may have similar free energy of formation to each other and compared to other transition metal oxides, the thermodynamic probability of the formation of one versus the other is similar [65]. Hence, the Cr_2O_3 and Mn oxides, whether MnO, Mn_3O_4 or Mn_2O_3 , likely exist as phase separated layers as seen during high temperature oxidation [37]. This situation is detrimental to corrosion resistance of an oxide film. Hence the Mn oxide formed on other MPEAs and steel surfaces are not protective in aqueous solutions [30, 31, 37].

425

426 *The role of other alloying elements*

Ni was observed to dissolve into solution and only minor or trace amounts of Fe and Co were found in oxides on the $Ni_{38}Fe_{20}Cr_{22}Mn_{10}Co_{10}$ MPEA (Figs. 4 and 5). The Fe 3p spectrum of

1
2
3 429 the $\text{Ni}_{38}\text{Fe}_{20}\text{Cr}_{22}\text{Mn}_{10}\text{Co}_{10}$ MPEA after $E_{\text{ap}} = 0.1$ V vs. SCE (Fig. 10(b)) showed metallic and oxide
4
5
6 430 state peaks at 52.8 eV and 55.2 eV, respectively. Fe dissolved congruently during AESEC-CA
7
8 431 experiments as shown in Fig. 4 and was estimated to be accumulated at the surface at
9
10 432 concentrations of only 50 ng cm^{-2} after 4000 s at both applied potentials (Fig. 5). A small amount
11
12 433 of oxidized Co is also seen in XPS 3p spectra. It is proposed here that remaining oxidized Fe and
13
14 434 Co might form spinels with Cr but these cannot be a source of protection as they could not account
15
16 435 for all the Cr which is oxidized and also would not be present in sufficient amount to cover the
17
18 436 surface. It should be also noted that an air-formed oxide possibly formed during sample transfer
19
20 437 to the XPS instrument. The Fe 3p oxide component after AESEC-CA experiments might be due
21
22 438 to the Fe-based oxide formation during sample transfer after polishing, which was not maintained
23
24 439 in a vacuum. Hence, the dominant oxides are Cr and Mn-rich and likely in a layered unmixed state
25
26 440 with dissolution of Fe, Ni, and Co.
27
28
29
30
31
32

33 442 **Conclusions**

- 35 443 • The fate of alloying elements during dissolution and passivation of the
36 444 $\text{Ni}_{38}\text{Fe}_{20}\text{Cr}_{22}\text{Mn}_{10}\text{Co}_{10}$ MPEA differs distinctly depending on the applied potential. Ni
37
38 445 dissolves at all potentials investigated in this work, Fe and Co are incorporated into oxides
39
40 446 or hydroxides in low concentrations, while Cr is enriched in the oxide at passive potentials.
41
42 447 Mn(II) both dissolves and is incorporated in minor amounts in oxides containing large
43
44 448 concentrations of Cr(III) at low passivating potential. Considerable presence of Mn(II) is
45
46 449 observed in the oxide relative to Cr(III) at $E_{\text{ap}} = 0.1$ V vs. SCE.
47
48
49
50
51
52 450 • It is posited that Mn has a detrimental effect on passivity of the $\text{Ni}_{38}\text{Fe}_{20}\text{Cr}_{22}\text{Mn}_{10}\text{Co}_{10}$
53
54 451 MPEA. The effect is potential-dependent and degrades the corrosion resistance of the
55
56
57
58
59
60

1
2
3 452 $\text{Ni}_{38}\text{Fe}_{20}\text{Cr}_{22}\text{Mn}_{10}\text{Co}_{10}$ MPEA compared to a $\text{Ni}_{78}\text{Cr}_{22}$ binary alloy in 0.1 M NaCl at pH =
4
5 453 4. EIS and DC electrochemical tests indicate that change in potential from 0.0 V to 0.1 V
6
7
8 454 vs. SCE is detrimental to corrosion resistance of the electrochemically formed passive film
9
10 455 compared to the $\text{Ni}_{78}\text{Cr}_{22}$ binary alloy.

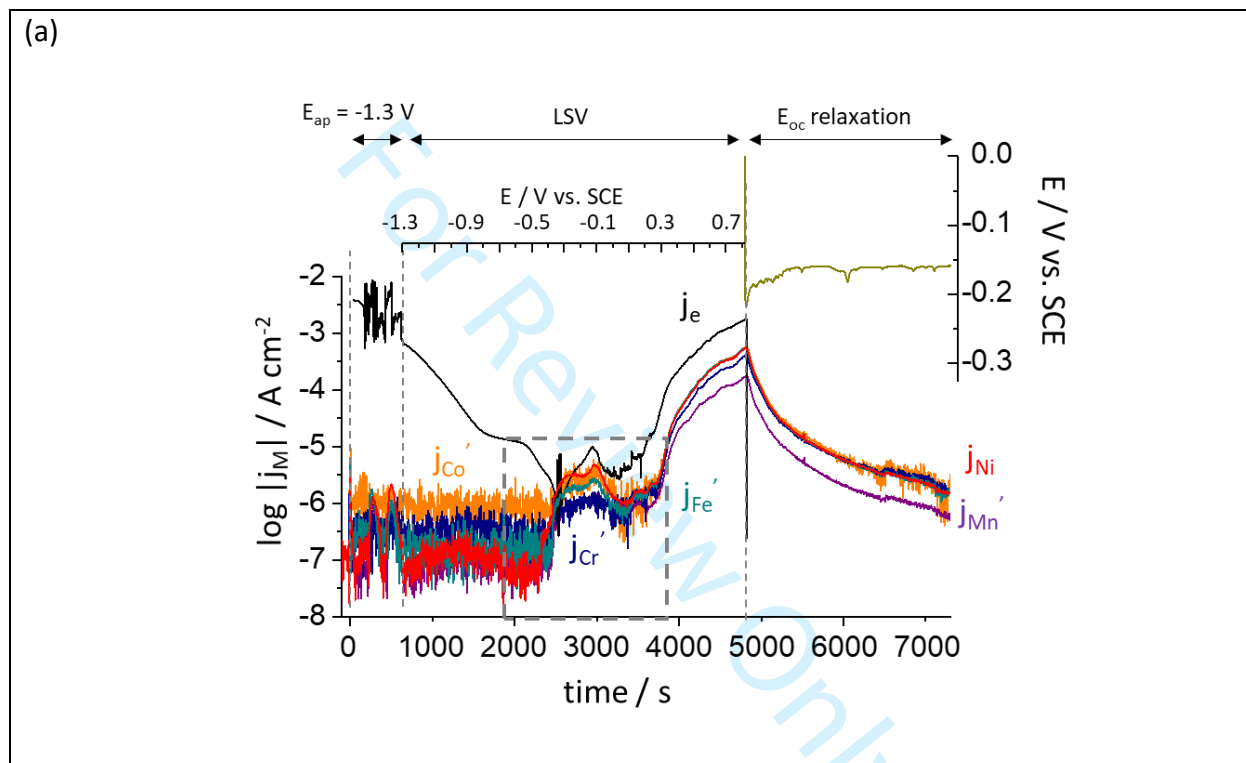
- 11
12 456 • The presence of Mn-based oxide was indicated indirectly by non-congruent dissolution in
13
14 457 AESEC results and corroborated by XPS spectra, including 3p core level analysis at $E_{\text{ap}} =$
15
16
17 458 0.1 V vs. SCE. This Mn-containing oxide layer was not as protective as the Cr-rich oxide
18
19 459 indicated by increasing elemental dissolution rates with time at this potential. A lower Z_{mod}
20
21 460 in the low-frequency EIS as well as lower inner oxide resistance obtained from a model
22
23 461 circuit fitting for the $\text{Ni}_{38}\text{Fe}_{20}\text{Cr}_{22}\text{Mn}_{10}\text{Co}_{10}$ MPEA at this potential are also indicative of
24
25 462 the less protective oxide. This was corroborated by j_e versus time in constant potential
26
27 463 experiments, which indicated increased anodic current densities and local breakdown in
28
29 464 the MPEA compared to the $\text{Ni}_{78}\text{Cr}_{22}$ binary alloy.
- 30
31 465 • For the $\text{Ni}_{38}\text{Fe}_{20}\text{Cr}_{22}\text{Mn}_{10}\text{Co}_{10}$ MPEA, a layered oxide is suggested by EIS and supported
32
33 466 by thermodynamic calculations when a constant potential is applied in the passive potential
34
35 467 domain. At $E_{\text{ap}} = 0.1$ V vs. SCE, a porous oxide is indicated and interpreted to occur by
36
37 468 selective dissolution of Ni, Fe, and Co leaving behind Cr and Mn-based oxide layers.
38
39
40
41
42
43
44
45

46 470 **Acknowledgement**

47
48 471 The research was primarily supported as part of the Center for Performance and Design of Nuclear
49
50 472 Waste Forms and Containers (WastePD), an Energy Frontier Research Center (ERFC) funded by
51
52 473 the U.S. Department of Energy (DOE), Office of Science, Basic Energy Sciences (BES), under
53
54 474 award #DE-SC0016584. Utilization of the PHI VersaProbe IIITM instrument was supported by
55
56
57
58
59
60

1
2
3 475 Nanoscale Materials Characterization Facility (NMCF) within University of Virginia funded by
4
5 476 NSF award (#162601) for acquisition of this instrument. K. Ogle and the AESEC experiments
6
7 477 were supported by the Agence Nationale de Recherche, grant # ANR-20-CE08-0031 (Tapas 2020).
8
9 478 Author X. Li is grateful to Chinese Scholarship Council (CSC) for the financial support.
10
11

12 479 **Figures**



39 **Fig. 1.** AESEC-LSV of the $\text{Ni}_{38}\text{Fe}_{20}\text{Cr}_{22}\text{Mn}_{10}\text{Co}_{10}$ MPEA in a deaerated 0.1 M NaCl, pH = 4
40 solution with 0.5 mV s^{-1} scan rate. Prior to the LSV measurement, a constant potential at $E_{\text{ap}} =$
41 -1.3 V vs. SCE was applied to reduce the pre-existing air-formed oxide. After the potential
42 release, elemental dissolution rates were recorded during open circuit measurement (E_{oc}
43 relaxation). Normalized elemental dissolution rates equivalent to current densities (j_{M}') using
44 Eq. 4 are given to demonstrate deviations from congruent dissolution.
45
46
47
48
49
50
51
52

53 480

54 481

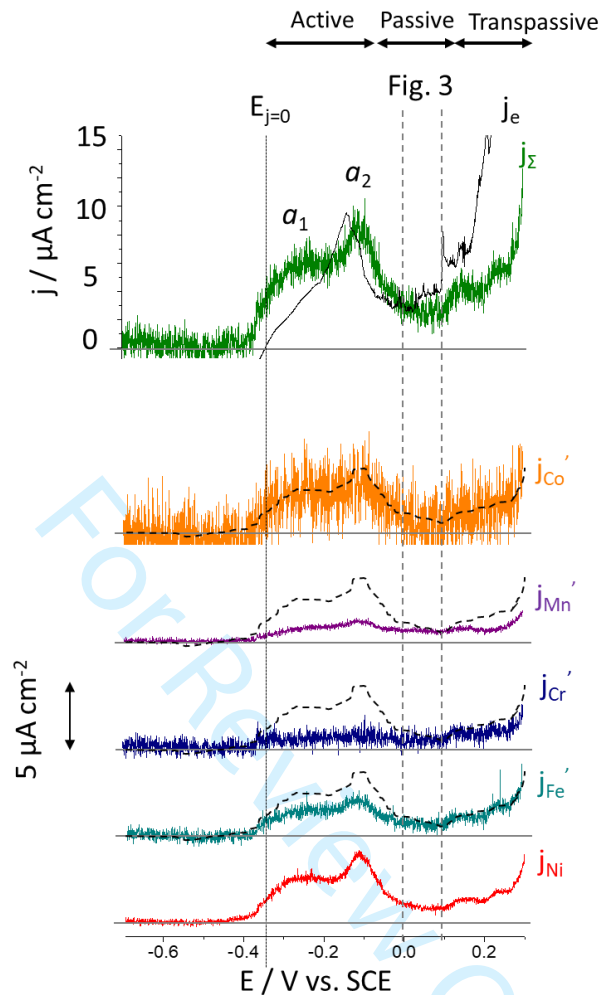


Fig. 2. Results from AESEC-LSV of the $\text{Ni}_{38}\text{Fe}_{20}\text{Cr}_{22}\text{Mn}_{10}\text{Co}_{10}$ MPEA in a deaerated 0.1 M NaCl, pH = 4 solution. j'_M , the sum of j_M (j_Σ) and electrical current density (j_e) magnified in the active and passive potential domain from Fig. 1 are presented. j'_M curves are given with offset. Horizontal lines indicate zero value ($j'_M = 0$). Dashed line indicates the j'_{Ni} to determine congruent dissolution of each alloying element. If j'_M equals to the dashed line, that may indicate congruent dissolution of M. If j'_M is lower than the dashed line, dissolution of M is non-congruent.

482
483
484

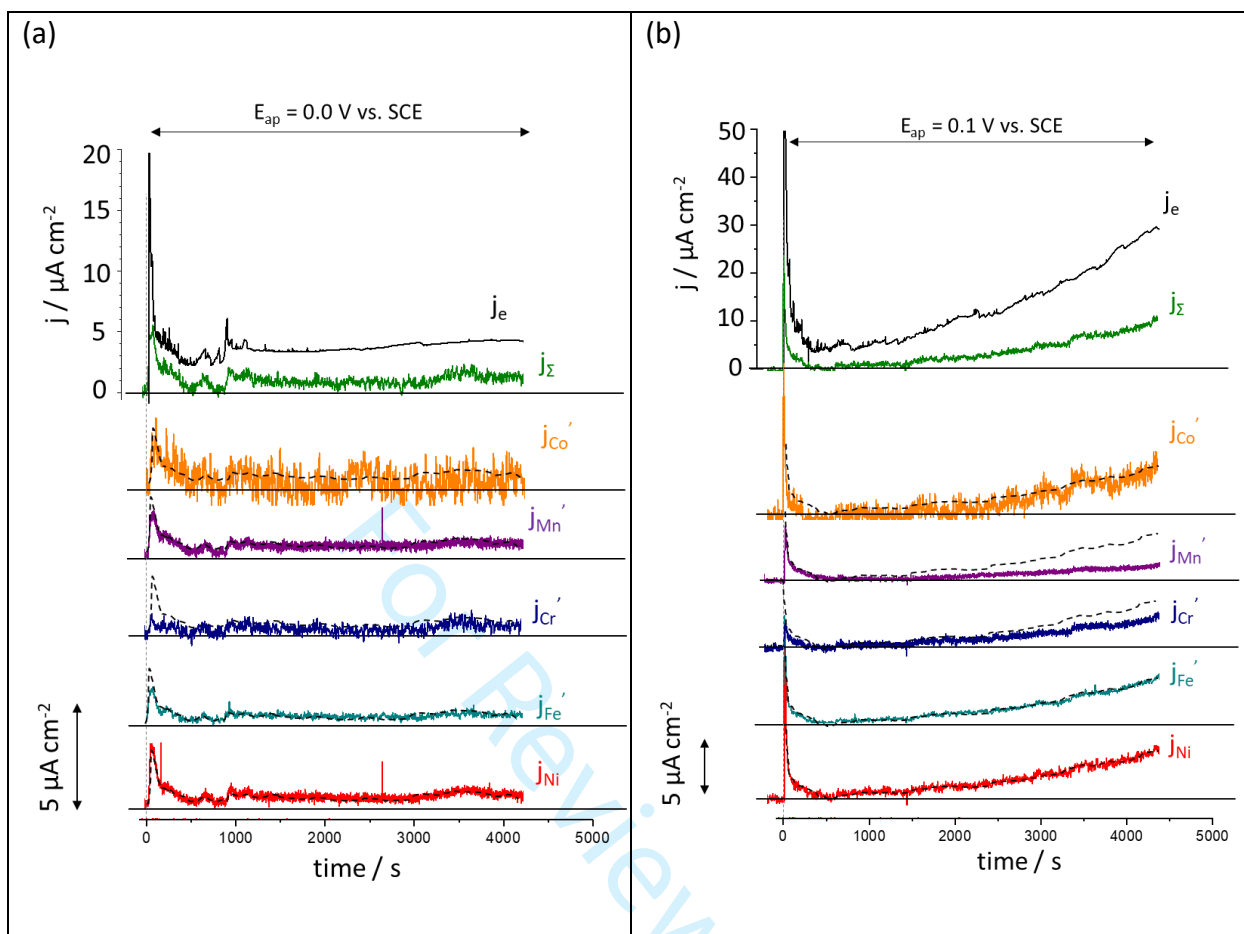


Fig. 3. AESEC chronoamperometry (AESEC-CA) of the $\text{Ni}_{38}\text{Fe}_{20}\text{Cr}_{22}\text{Mn}_{10}\text{Co}_{10}$ MPEA at a passive potential; **(a)** $E_{\text{ap}} = 0.0$ V, and **(b)** $E_{\text{ap}} = 0.1$ V vs. SCE in 0.1 M NaCl, pH = 4.0, deaerated solution, after a cathodic reduction at $E_{\text{ap}} = -1.3$ V vs. SCE for 600 s. The vertical dashed line indicates $t = 0$ when the potentiostatic hold started after the cathodic reduction step.

485
486
487
488
489
490
491
492
493
494
495
496

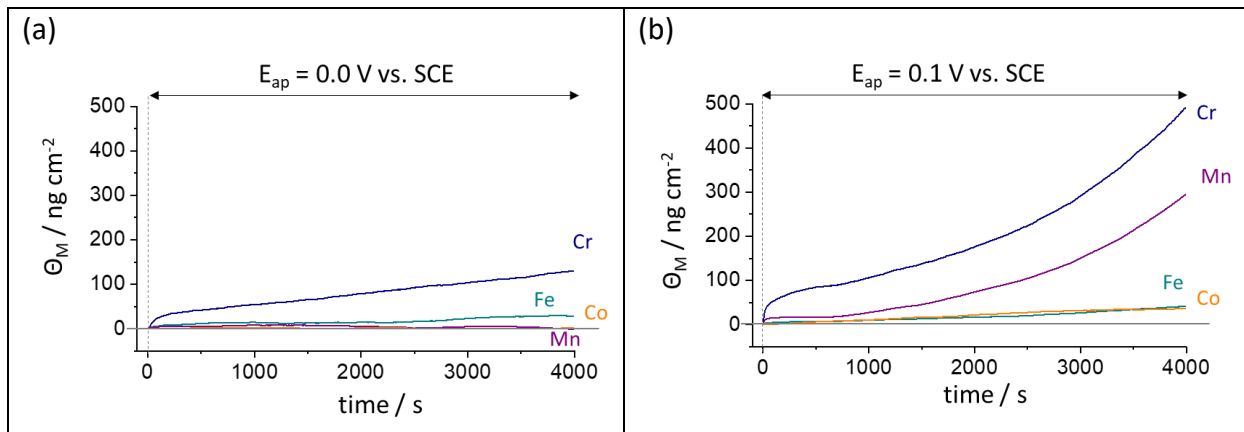
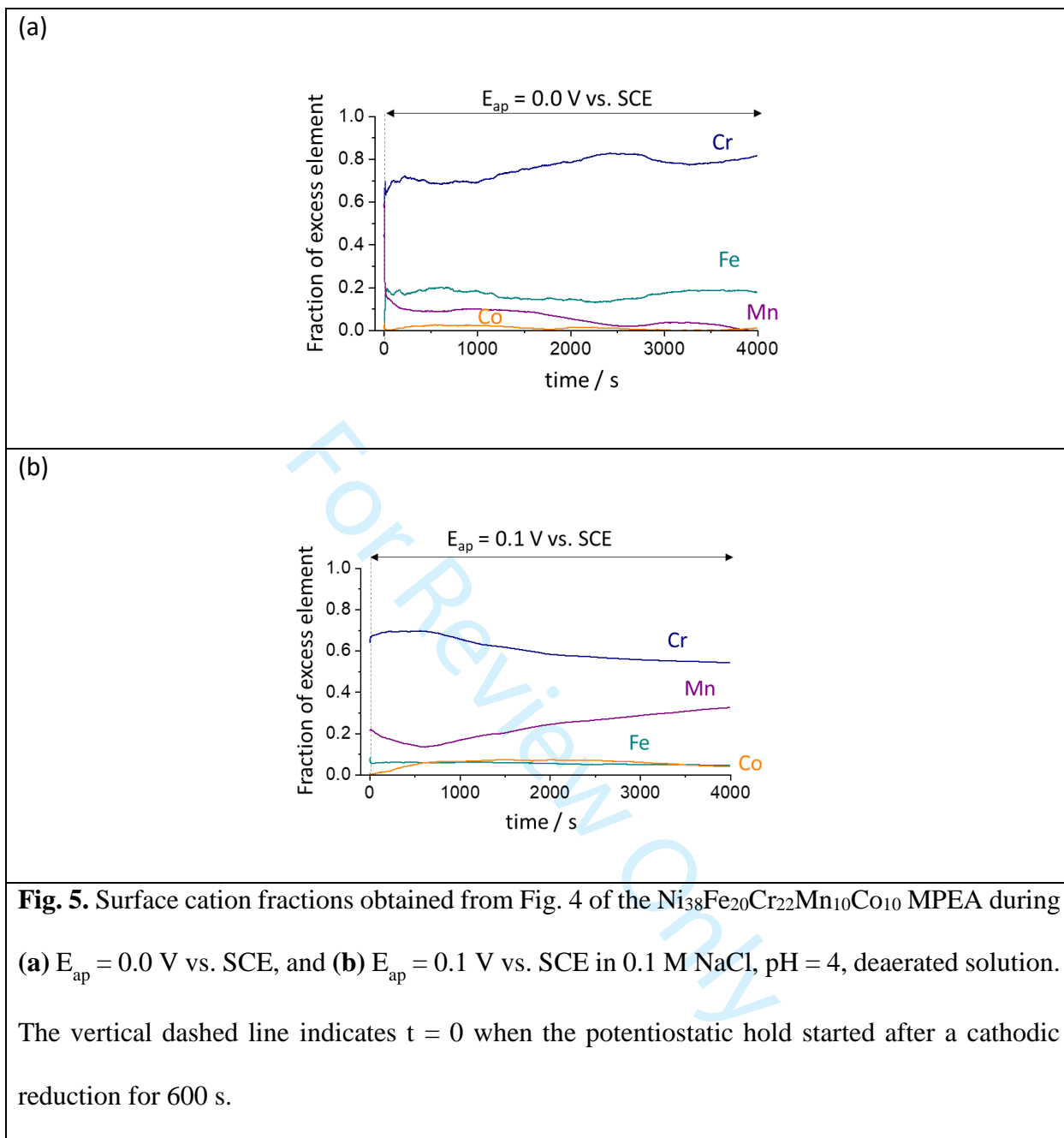
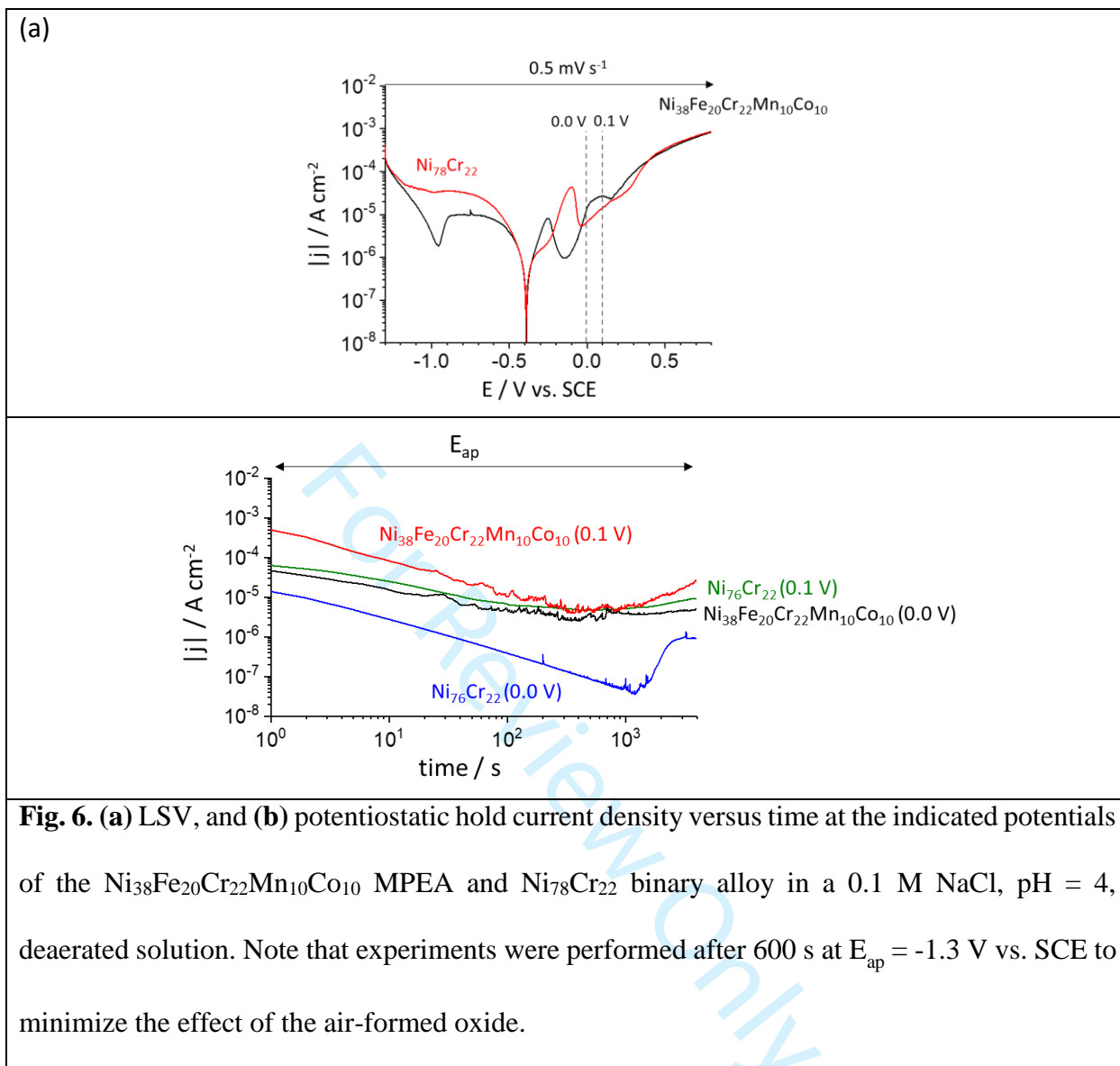


Fig. 4. The excess element M (Θ_M) in ng cm^{-2} oxidized and residing in solid form at the alloy surface calculated by a mass-balance (Eq. 6) during each AESEC-CA experiment from Fig. 3; **(a):** $E_{\text{ap}} = 0.0 \text{ V vs. SCE}$ and **(b):** $E_{\text{ap}} = 0.1 \text{ V vs. SCE}$. The vertical dashed line is $t = 0$ when the potentiostatic hold started after a cathodic reduction for 600 s.

497
498
499
500
501
502
503
504
505
506
507
508
509
510
511
512
513
514
515
516
517
518
519
520
521



522
523
524
525
526
527
528
529
530
531



532
533
534
535
536

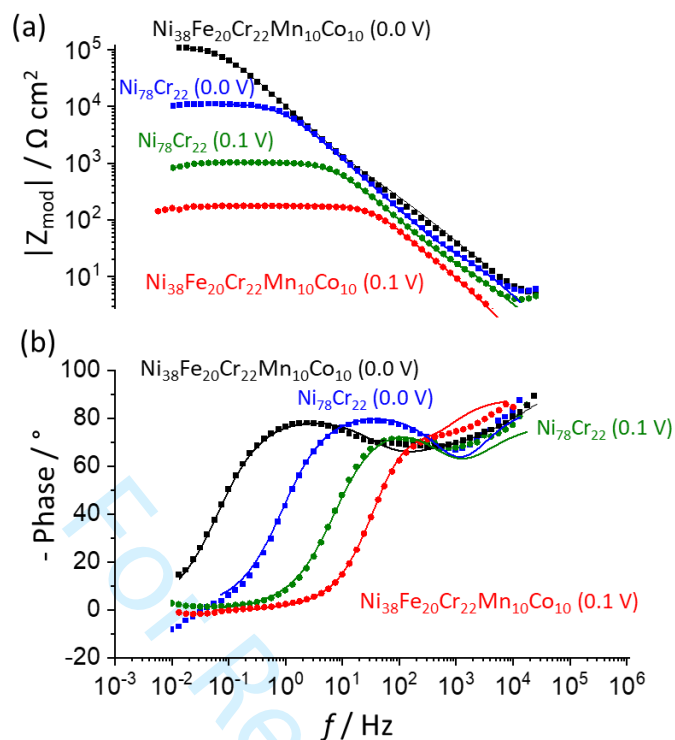
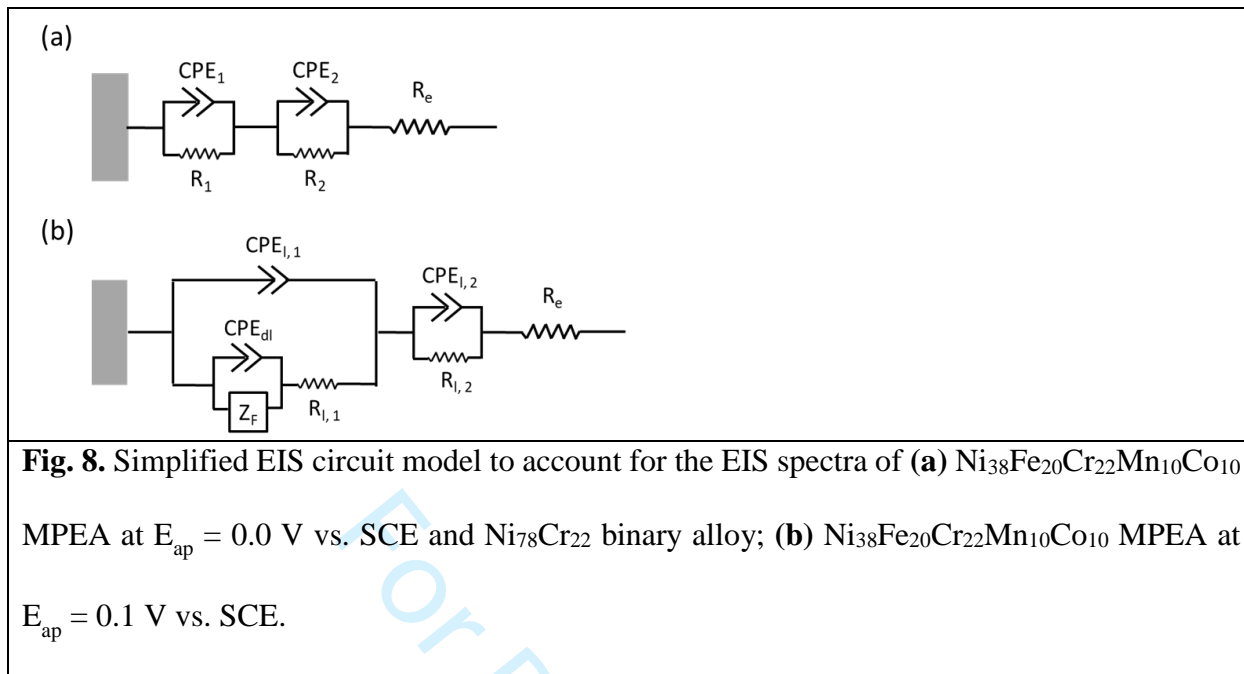
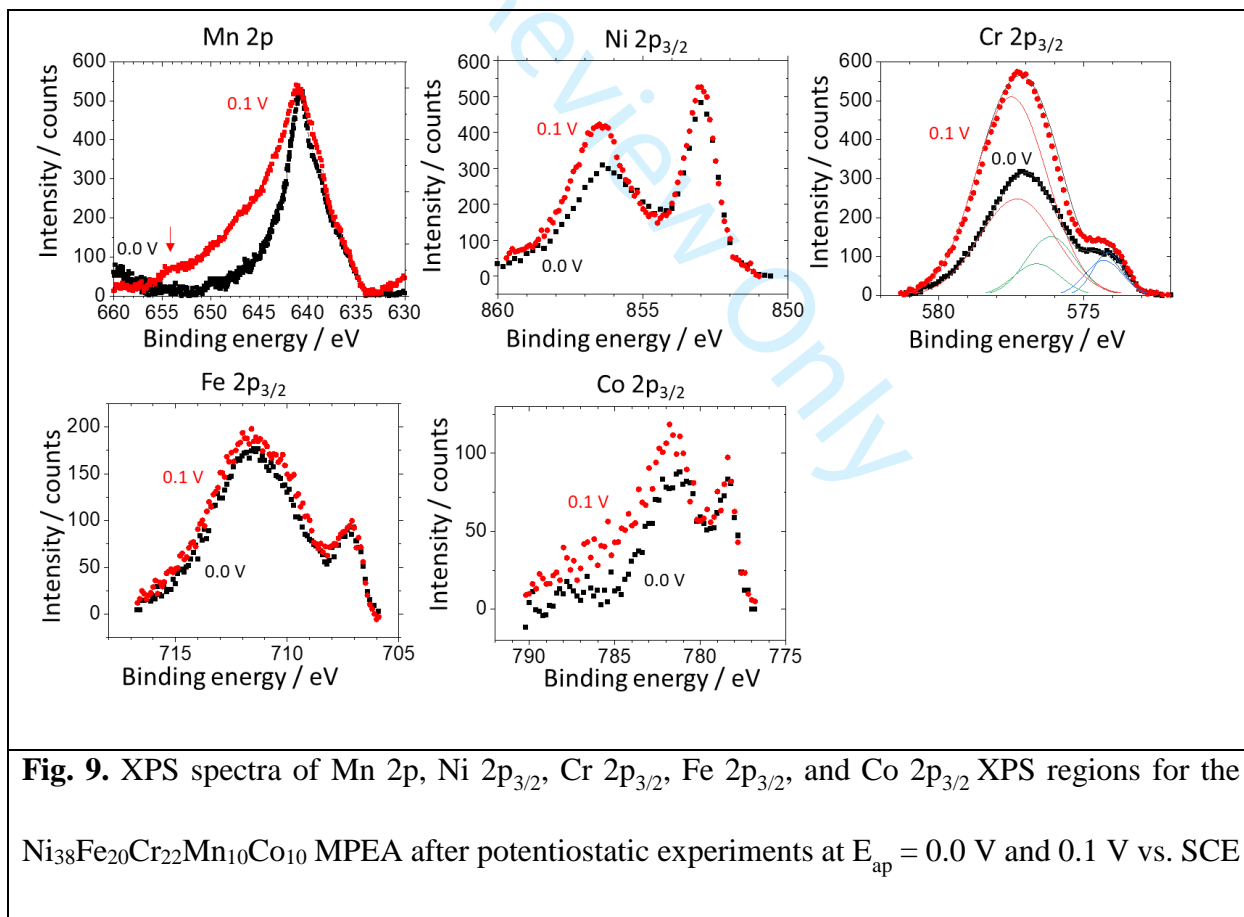


Fig. 7. (a) Bode magnitude, and **(b)** phase plot after each 4000 s potentiostatic hold on the $\text{Ni}_{38}\text{Fe}_{20}\text{Cr}_{22}\text{Mn}_{10}\text{Co}_{10}$ MPEA and $\text{Ni}_{78}\text{Cr}_{22}$ binary alloy, following a cathodic reduction at $E_{\text{ap}} = -1.3$ V vs. SCE for 600 s. Equivalent circuits used to fit the EIS spectra are given in Fig. 8 and the fitting results are shown by solid lines while the symbols represent the data points.

537
538
539
540
541
542
543



544



for 4000 s in 0.1 M NaCl, pH = 4.0, deaerated solution followed by an air transfer for XPS analysis.

545

546

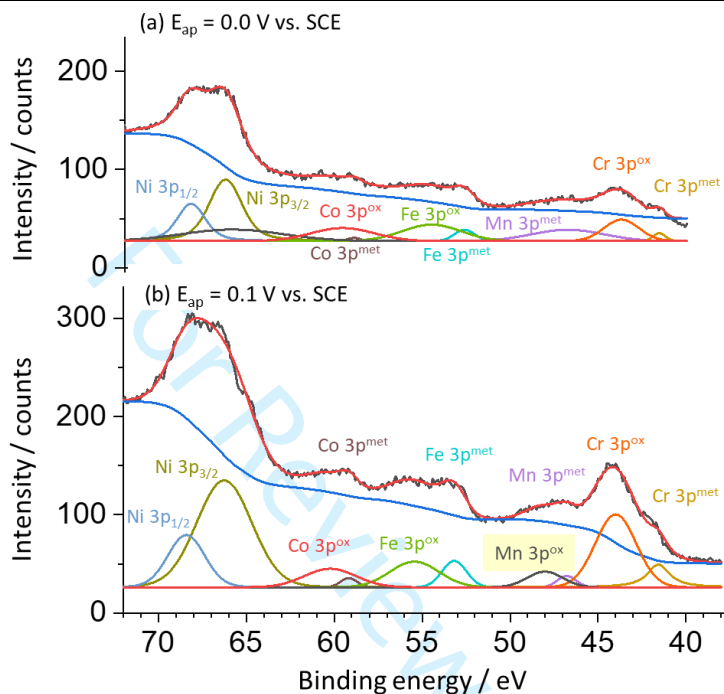


Fig. 10. XPS 3p core level spectra of Ni, Fe, Cr, Mn and Co after potentiostatic hold experiments on the Ni₃₈Fe₂₀Cr₂₂Mn₁₀Co₁₀ MPEA at (a) $E_{ap} = 0.0$ V vs. SCE, and (b) $E_{ap} = 0.1$ V vs. SCE for 4000 s in 0.1 M NaCl, pH = 4.0 deaerated solution.

547

548

549

550

551

552

553

554

555

556

557

558 **References**

- [1] D.B. Miracle, and O.N. Senkov, "A critical review of high entropy alloys and related concepts", *Acta Mat.*, **122**, 448-511 (2017). <http://dx.doi.org/10.1016/j.actamat.2016.08.081>.
- [2] R. Feng, M.C. Gao, C. Lee, M. Mathes, T. Zuo, S. Chen, J.A. Hawk, Y. Zhang, and P.K. Liaw, "Design of light-weight high-entropy alloys", *Entropy-Switz*, **18**, 333 (2016). <https://doi.org/10.3390/e18090333>.
- [3] T.H. Tsai, and J.W. Yeh, "High-entropy alloys: A critical review", *Mater. Res. Lett.*, **2** (2014) 107–123. <http://dx.doi.org/10.1016/j.actamat.2013.04.058>.
- [4] Y. Qiu, M.A. Gibson, H.L. Fraser, and N. Birbilis, "Corrosion characteristics of high entropy alloys", *Mat. Sci. and Tech.*, **31** (2015) 1235-124. <https://doi.org/10.1179/1743284715Y.0000000026>.
- [5] G.S. Frankel, J. Vienna, and J. Lian, "WastePD, an innovative center on materials degradation", *npj Materials Degradation*, **1:5** (2017). <https://doi.org/10.1038/s41529-017-0002-5>.
- [6] L.J. Santodonato, Y. Zhang, M. Feygenson, C.M. Parish, M.C. Gao, R.J. Weber, J.C. Neuefeind, Z. Tang, P.K. Liaw, "Deviation from high-entropy configurations in the atomic distributions of a multi-principal-element alloy", *Nature Communications*, **6**, 5964 (2015). <https://doi.org/10.1038/ncomms6964>.
- [7] J-W. Yeh, S-J. Lin, "Breakthrough applications of high-entropy materials", *J. Mat. Research*, **33**(19), 3129-3137 (2018). <https://doi.org/10.1557/jmr.2018.283>.
- [8] P. Lu, J.E. Saal, G.B. Olson, T.S. Li, O.J. Swanson, G.S. Frankel, A.Y. Gerard, K.F. Quiambao, and J.R. Scully, "Computational materials design of a corrosion resistant high entropy alloy for harsh environments", *Scripta Mater.*, **153** (2018) 19-22. <https://doi.org/10.1016/j.scriptamat.2018.04.040>.
- [9] P. Lu, J.E. Saal, G.B. Olson, T. Li, S. Sahu, O.J. Swanson, G.S. Frankel, A.Y. Gerard, and J.R. Scully, "Computational design and initial corrosion assessment of a series of non-equimolar high entropy alloys", *Scripta Mater.*, **172** (2019) 12-16. <https://doi.org/10.1016/j.scriptamat.2019.07.003>.
- [10] J.R. Scully, S.B. Inman, A.Y. Gerard, C.D. Taylor, W. Windl, D.K. Schreiber, P. Lu, J.E. Saal, and G.S. Frankel, "Controlling the corrosion resistance of multi-principal element alloys", *Scripta Mat.*, **188**, 96-101 (2020). <https://doi.org/10.1016/j.scriptamat.2020.06.065>.
- [11] C.D. Talor, P. Lu, J. Saal, G.S. Frankel, and J.R. Scully, "Integrated computational materials engineering of corrosion resistant alloys", *npj Materials Degradation*, **2:6** (2018). <https://doi.org/10.1038/s41529-018-0027-4>.
- [12] Z. Cui, Z. Qin, P. Dong, Y. Mi, D. Gong, and W. Li, "Microstructure and corrosion properties of FeCoNiCrMn high entropy alloy coating prepared by high speed laser cladding and ultrasonic surface mechanical rolling treatment", *Mat. Letters*, **259**, 126768 (2020). <https://doi.org/10.1016/j.matlet.2019.126769>.
- [13] G.R. Holcomb, J. Tylczak, and C. Carney, "Oxidation of CoCrFeMnNi high entropy alloys", *JOM*, **67**(10), 2326-2339 (2015). <https://doi.org/10.1007/s11837-015-1517-2>.
- [14] Y.-K. Kim, Y.-A. Joo, H.S. Kim, and K.-A. Lee, "High temperature oxidation behavior of Cr-Mn-Fe-Co-Ni high entropy alloy", *Intermetallics*, **98**, 45-53 (2018). <https://doi.org/10.1016/j.intermet.2018.04.006>.
- [15] T. Nagase, T. Kakeshita, K. Matsumura, K. Nakazawa, S. Furuya, N. Ozoe, and K. Yoshino, "Development of Fe-Co-Cr-Mn-Ni high entropy case iron (HE cast iron) available for casting in air atmosphere", *Materials and Design*, **184**, 108172 (2018). <https://doi.org/10.1016/j.matdes.2019.108172>.
- [16] C. Wang, J. Yu, Y. Yu, Y. Zhao, Y. Zhang, and X. Han, "Comparison of the corrosion and passivity behavior between CrMnFeCoNi and CrFeCoNi coatings prepared by argon arc cladding", *J. Mat. Res. Technol.*, **9**(4), 8482-8496 (2020). <https://doi.org/10.1016/j.jmrt.2020.05.093>.
- [17] Q. Ye, K. Feng, Z. Li, F. Lu, R. Li, J. Huang, and Y. Wu, "Microstructure and corrosion properties of CrMnFeCoNi high entropy alloy coating", *Appl. Surf. Sci.*, **396**, 1420-1426 (2017). <http://dx.doi.org/10.1016/j.apsusc.2016.11.176>.

- [18] K.F. Quiambao, S.J. McDonnell, D.K. Schreiber, A.Y. Gerard, K.M. Freedy, P. L.u, J.E. Saal, G.S. Frankel, and J.R. Scully, "Passivation of a corrosion resistant high entropy alloy in non-oxidizing sulfate solutions", *Acta Mat.*, **164** (2019) 362-376. <https://doi.org/10.1016/j.actamat.2018.10.026>.
- [19] T. Li, O. J. Swanson, G.S. Frankel, A.Y. Gerard, P. Lu, J.E. Saal, and J.R. Scully, "Localized corrosion behavior of a single-phase non-equimolar high entropy alloy", *Electrochim. Acta*, **306** (2019) 71-84. <https://doi.org/10.1016/j.electata.2019.03.104>.
- [20] D. Hamm, K. Ogle, C.-O. A. Olsson, S. Weber, and D. Landolt, "Passivation of Fe-Cr alloys studied with ICP-AES and EQCM", *Corros. Sci.*, **44** (2002) 1443-1456. [https://doi.org/10.1016/S0010-938X\(01\)00147-0](https://doi.org/10.1016/S0010-938X(01)00147-0).
- [21] K.L. Cwalina, H.M. Ha, N. Ott, P. Reinke, N. Birbilis, and J.R. Scully, "In operando analysis of passive film growth on Ni-Cr and Ni-Cr-Mo alloys in chloride solutions", *J. Electrochem. Soc.*, **166**(11) C3241-C3253 (2019). <https://doi.org/10.1149/2.0261911jes>.
- [22] X. Li, and K. Ogle, "The passivation of Ni-Cr-Mo alloys: Time resolved enrichment and dissolution of Cr and Mo during passive-active cycles", *J. Electrochem. Soc.*, **166**(11) C3179-C3185 (2019). <https://doi.org/10.1149/2.0201911jes>.
- [23] A. Ferrari, and F. Körmann, "Surface segregation in Cr-Mn-Fe-Co-Ni high entropy alloys", *Appl. Surf. Sci.*, **533**, 147471 (2020). <https://doi.org/10.1016/j.apsusc.2020.147471>.
- [24] K. Wang, J. Han, A.Y. Gerard, J.R. Scully, and B.-C. Zhou, "Potential-pH diagrams considering complex oxide solution phase for understanding aqueous corrosion of multi-principal element alloys", *npj Mat. Deg.*, 4:35 (2020). <https://doi.org/10.1038/s41529-020-00141-6>.
- [25] H. Luo, Z. Li, A. M. Mingers, D. Raabe, "Corrosion behavior of an equiatomic CoCrFeMnNi high-entropy alloy compared with 304 stainless steel in sulfuric acid solution", *Corros. Sci.*, **134**, 131-139 (2018). <https://doi.org/10.1016/j.corsci.2018.02.031>.
- [26] H. Torbati-Sarraf, M. Shabani, P.D. Jablonski, G.J. Pataky, and A. Poursaeed, "The influence of incorporation of Mn on the pitting corrosion performance of CrFeCoNi high entropy alloy at different temperature", *Mat. & Design*, **18**, 108170 (2019). <https://doi.org/10.1016/j.matdes.2019.108170>.
- [27] J. Yang, J. Wu, C.Y. Zhang, S.D. Zhang, B.J. Yang, W. Emori, and J.Q. Wang, "Effects of Mn on the electrochemical corrosion and passivation behavior of CoFeNiMnCr high-entropy alloy system in H₂SO₄ system", *J. Alloys and Compounds*, **819**, 152943 (2020). <https://doi.org/10.1016/j.jallcom.2019.152943>.
- [28] A.Y. Gerard, J. Han, S.J. McDonnell, K. Ogle, E.J. Kautz, D.K. Schreiber, J.E. Saal, G.S. Frankel, and J.R. Scully, "Aqueous passivation of multi-principal element alloy Ni₃₈Fe₂₀Cr₂₂Mn₁₀Co₁₀: Unexpected high Cr enrichment within the passive film", *Acta Materialia*, **198**, 121-133 (2020). <https://doi.org/10.1016/j.actamat.2020.07.024>.
- [29] A. Rodriguez, J.H. Tylczak, and M. Ziomek-Moroz, "Corrosion behavior of CoCrFeMnNi high-entropy alloys (HEAs) under acidic aqueous conditions", *ECS Trans.*, 77(11), 741-752 (2017). <https://doi.org/10.1149/07711.0741ecst>.
- [30] M. Kim and J. Kim, "Effect of manganese on the corrosion behavior of low carbon steel in 10 wt.% sulfuric acid", *Int. J. Electrochem. Sci.*, **10** (2015) 6872-6885.
- [31] K. Park, and H. Kwon, "Effect of Mn on the localized corrosion behavior of Fe-18Cr alloys", *Electrochim. Acta*, **55** (2010) 3421-3427. <https://doi.org/10.1016/j.electata.2010.01.006>.
- [32] G. Wranglén "Pitting and sulphide inclusions in steel", *Corros. Sci.*, **14** (1974) 331-349. [https://doi.org/10.1016/S0010-938X\(74\)80047-8](https://doi.org/10.1016/S0010-938X(74)80047-8).
- [33] E.G. Webb, T. Suter, and R.C. Alkire, "Microelectrochemical measurements of the dissolution of single MnS inclusions, and the prediction of the critical conditions for pit initiation on stainless steel", *J. Electrochem. Soc.*, **148**(5) B186-B195 (2001). <https://doi.org/10.1149/1.1360205>.
- [34] S. Fajardo, I. Lorente, J.A. Jiménez, J.M. Bastidas, and D.M. Bastidas, "Effect of Mn additions on the corrosion behaviour of TWIP Fe-Mn-Al-Si austenitic steel in chloride solution", *Corros. Sci.*, **154**, 246-253 (2019). <https://doi.org/10.1016/j.corsci.2019.04.026>.

- [35] T.D. Nguyen, J. Zhang, and D.J. Young, "Effect of Mn on oxide formation by Fe-Cr and Fe-Cr-Ni alloys in dry and wet CO₂ gases at 650°C", *Corros. Sci.*, **112**, 110-127 (2016). <http://dx.doi.org/10.1016/j.corsci.2016.07.014>.
- [36] G. Laplanche, U.F. Volkert, G. Eggeler, and E.P. George, "Oxidation behavior of the CrMnFeCoNi high-entropy alloy", *Oxid. Met.*, **85**, 629-645 (2016). <https://doi.org/10.1007/s11085-016-9616-1>.
- [37] F.H. Stott, F.I. Wei, and C.A. Enahoro, "The influence of manganese on the high-temperature oxidation of iron-chromium alloys", *Werkstoffe und Korrosion*, **40**, 198-208 (1989). <https://doi.org/10.1002/mac0.19890400403>.
- [38] R. K. Wild, "High temperature oxidation of austenitic stainless steel in low oxygen pressure", *Corros. Sci.*, **17**, 87-104 (1977). [https://doi.org/10.1016/0010-938X\(77\)90011-7](https://doi.org/10.1016/0010-938X(77)90011-7).
- [39] W. Sun, D. A. Kitchaev, D. Kramer, and G. Ceder, "Non-equilibrium crystallization pathways of manganese oxide in aqueous solution", *Nature Commun.*, 10:573 (2019). <https://doi.org/10.1038/s41467-019-08484-6>.
- [40] K. Ogle, M. Mokaddem, and P. Volovitch, "Atomic emission spectroelectrochemistry applied to dealloying phenomena II. Selective dissolution of iron and chromium during active-passive cycles of an austenitic stainless steel", *Electrochem. Acta*, **55**(3), 913-921 (2010). <https://doi.org/10.1016/j.electroacta.2009.08.028>.
- [41] L. Wang, D. Mercier, S. Zanna, A. Seyeux, M. Laurent-Brocq, L. Perrière, I. Guillot, and P. Marcus, "Study of the surface oxides and corrosion behaviour of an equiatomic CoCrFeMnNi high entropy alloy by XPS and ToF-SIMS", *Corros. Sci.*, 167, 108507 (2020). <https://doi.org/10.1016/j.corsci.2020.108507>.
- [42] J. Han, D. Thierry, and K. Ogle, "Zr-based conversion coating on Zn and Zn-Al-Mg alloy coating: Understanding the accelerating effect of Cu(II) and NO₃⁻", *Surf. & Coat. Tech.*, **402**, 126236 (2020). <https://doi.org/10.1016/j.surfcoat.2020.126236>.
- [43] K.L. Cwalina, H.M. Ha, N. Ott, P. Reinke, N. Birbilis, and J.R. Scully, "In operando analysis of passive film growth on Ni-Cr and Ni-Cr-Mo alloy in chloride solutions", *J. Electrochem. Soc.*, **166**(11), C32410C3253 (2019). <https://doi.org/10.1149/2.0261911jes>.
- [44] J.D. Henderson, X. Li, D.W. Shoesmith, J.J. Noël, and K. Ogle, "Molybdenum surface enrichment and release during transpassive dissolution of Ni-based alloys", *Corros. Sci.*, **147**, 32-40 (2019). <https://doi.org/10.1016/j.corsci.2018.11.005>.
- [45] K. Ogle, "Atomic emission spectroelectrochemistry: Real-time rate measurements of dissolution, corrosion, and passivation", *Corrosion*, **75**(12), 1398-1419 (2019). <https://doi.org/10.5006/3336>.
- [46] X. Li, J.D. Henderson, F.P. Filice, D. Zagidulin, M.C. Biesinger, F. Sun, B. Qian, D.W. Shoesmith, J.J. Noël, and K. Ogle, "The contribution of Cr and Mo to the passivation of Ni₂₂Cr and Ni₂₂Cr₁₀Mo alloys in sulfuric acid", *Corros. Sci.*, **176**, 109015 (2020). <https://doi.org/10.1016/j.corsci.2020.109015>.
- [47] Y. Qiu, R. Liu, T. Gengenbach, O. Gharbi, S. Choudhary, S. Thomas, H.L. Fraser, and N. Birbilis, "Real-time dissolution of a compositionally complex alloy using inline ICP and correlation with XPS", *npj Mat. Degrad.*, 4:7 (2020). <https://doi.org/10.1038/s41629-020-0112-3>.
- [48] S. Choudhary, Y. Qiu, S. Thomas, and N. Birbilis, "Element-resolved electrochemical analysis of transpassive dissolution and repassivation behavior of the multi-principle element alloy AlTiVCr", *Electrochim. Acta*, **362**, 137104 (2020). <https://doi.org/10.1016/j.electacta.2020.137104>.
- [49] X. Li, J. Han, P. Lu, J.E. Saal, G.B. Olson, G.S. Frankel, J.R. Scully, K. Ogle, "Dissolution and passivation of a Ni-Cr-Fe-Ru-Mo-W high entropy alloy by elementally resolved electrochemistry", *J. Electrochem. Soc.*, **167** (2020) 061505. <https://doi.org/10.1149/1945-7111/ab7f86>.
- [50] K. Ogle, and S. Weber, "Anodic dissolution of 304 stainless steel using atomic emission spectroelectrochemistry", *J. Electrochem. Soc.*, **147**(5) 1770-1780 (2000). <https://doi.org/10.1149/1.1393433>.
- [51] P. Lodi, K. Ogle, A. Storhaye, "Méthode d'analyse d'un échantillon métallique par dissolution de sa surface, et dispositif pour sa mise en œuvre", Patent, 92-3782, France (1992).
- [52] M.E. Orazem, N. Pébère, and B. Tribollet, "Enhanced graphical representation of electrochemical impedance data", *J. Electrochem. Soc.*, **153**(4), B129-B136 (2006). <https://doi.org/10.1149/1.2168377>.

- 1
2
3
4
5 [53] J. Han, and K. Ogle, "The anodic and cathodic dissolution of α -phase Zn-68Al in alkaline media", *Corros. Sci.*, **148**, 1-11 (2019). <https://doi.org/10.1016/j.corsci.2018.11.033>.
- 6
7 [54] Y.J. Li, A. Savan, K. Kostka, H.S. Stein, and A. Ludwig, "Accelerated atomic-scale exploration of
8 phase evolution in compositionally complex materials", *Mater. Hori.*, **5**, 86-92 (2018).
9 <https://doi.org/10.1039/c7mh00486a>.
- 10 [55] E.J. Kautz, S.V. Lambeets, D.E. Perea, A.Y. Gerard, J. Han, J.R. Scully, J.E. Saal, and D.K.
11 Schreiber, "Element redistributions during early stage of oxidation in a Ni₃₈Cr₂₂Fe₂₀Mn₁₀Co₁₀ multi-
12 principal element alloy", *Scripta Mat.*, **194**, 113609 (2021).
13 <https://doi.org/10.1016/j.scriptamat.2020.10.051>.
- 14 [56] P. Jakupi, D. Zagidulin, J.J. Noël, and D.W. Shoesmith, "The impedance properties of the oxide film
15 on the Ni-Cr-Mo alloy-22 in neutral concentrated sodium chloride solution", *Electrochim. Acta*, **56**, 6251-
16 6259 (2011). <https://doi.org/10.1016/j.electacta.2010.07.064>.
- 17 [57] J.D. Henderson, B. Almusned, M. Momeni, S. Anderson, V. Dehnavi, D. Zagidulin, D.W. Shoesmith,
18 and J.J. Noël, "Investigating the influence of Cr and Mo additions to commercial Ni-based alloys exposed
19 to neutral and acidic chloride solutions", *J. Electrochem. Soc.*, **167**, 131512 (2020).
20 <https://doi.org/10.1149/1945-711/abbea7>.
- 21 [58] I. Epelboin, M. Keddam, and J.C. Lestrade "Faradaic impedance and intermediates in electrochemical
22 reactions", *Faraday Discuss. Chem. Soc.*, **56**, 264-275 (1973). <https://doi.org/10.1149/1.3077576>.
- 23 [59] M.E. Orazem, and B. Tribollet, "Electrochemical impedance spectroscopy", *John Wiley & Sons*, 2nd
24 Ed., 201-205 (2017).
- 25 [60] M.C. Biesinger, B.P. Payne, A.P. Grosvenor, L.W.M. Lau, A.R. Gerson, R. St.C. Smart, "Resolving
26 surface chemical states in XPS analysis of first row transition metals, oxides and hydroxides: Cr, Mn, Fe,
27 Co, and Ni", *Appl. Surf. Sci.*, **257**, 2717-2730 (2011). <http://doi:10.1016/j.apsusc.2010.10.051>.
- 28 [61] H.W. Nesbitt, and D. Banerjee, "Interpretation of XPS Mn(2p) spectra of Mn oxyhydroxides and
29 constraints on the mechanism of MnO₂ precipitation", *American Mineralogist*, **83**, 305-315 (1998).
- 30 [62] A. Ramírez, P. Hilebrand, D. Stellmach, M.M. May, P. Bogdanoff, and S. Fiechter, "Evaluation of
31 MnO_x, Mn₂O₃, and Mn₃O₄ electrodeposited films for the oxygen evolution reaction of water", *J. Phys.*
32 *Chem. C*, **118**(26), 14073-14081 (2014). <https://doi.org/10.1021/jp500939d>.
- 33 [63] V. Di Castro, and G. Polzonetti, "XPS study of MnO oxidation", *J. Electron Spectroscopy and related*
34 *Phenomena*, **48**(1), 117-123 (1989). [https://doi.org/10.1016/0368-2048\(89\)80009-X](https://doi.org/10.1016/0368-2048(89)80009-X).
- 35 [64] E.S. Ilton, J.E. Post, P.J. Heaney, F.T. Ling, and S.N. Kerisit, "XPS determination of Mn oxidation
36 states in Mn (hydro)oxides", *Appl. Surf. Sci.*, **366**, 475-485 (2016).
37 <http://dx.doi.org/10.1016/j.apsusc.2015.12.159>.
- 38 [65] L.-F. Huang, and J.M. Rondinelli, "Reliable electrochemical phase diagrams of magnetic transition
39 metals and related compounds from high throughput ab initio calculations", *npj Mat. Deg.*, 3:26 (2019).
40 <https://doi.org/10.1038/s41529-019-0088-z>.
- 41
42
43
44
45
46
47
48
49
50
51
52
53
54
55
56
57
58
59
60